universität wien

# MASTERARBEIT / MASTER THESIS

Titel der Masterarbeit / Title of the Master's Thesis

## Diagnostic wind-downscaling with a mass consistent model using $\eta$ coordinates


verfasst von / submitted by

Maria Wind, B. Sc.


angestrebter akademischer Grad / in partial fulfilment of the requirements for the degree of

Master of Science (M. Sc.)

Wien, 2016 / Vienna, 2016

| | |
|---|---|
| Studienkennzahl lt. Studienblatt / degree programme code as it appears on the student record sheet: | A 066 614 |
| Studienrichtung lt. Studienblatt / degree programme as it appears on the student record sheet: | Meteorologie |
| Betreut von / Supervisor: | Ao. Univ.-Prof. Dr. Leopold Haimberger |

# Abstract

Resolving small scale wind fields on high resolution topography is still a challenging task, especially over complex terrain. In this work a mass consistent model using a pressure based terrain following vertical coordinate, the $\eta$ coordinate, is developed. At first the model is tested in an idealized simulation and then applied to real data. As input a 4 km WRF (Weather Research and Forecasting) simulation is used. This wind field is then downscaled to a 500 m grid with more detailed topographic information and adjusted to fulfil mass conservation. To evaluate the performance of the model, four case studies in an area with very complex terrain, a region around Innsbruck, Austria, are conducted. For verification, the results of the mass consistent model are compared to near-ground observations. Additionally, comparisons are made with a prognostic model with a resolution of 1 km which was available for the last case. To find the ideal value for the vertical transmission coefficient $\alpha_\eta$ which significantly influences the resulting fields, different empirical values are applied. Furthermore, formulas that link $\alpha_\eta$ to stability and standard deviation of the input wind field are used and the results analyzed.

Overall, the performance of the mass consistent model strongly depends on the quality and resolution of the input data, the prevailing weather conditions and the choice of $\alpha_\eta$. Best results are achieved for stable stratification during day time when strong synoptic forcing is present. The improvement compared to the 4 km-model is highest in terms of wind direction where the root mean square error (RMSE) can be reduced by up to 30°. However, decreasing the error in wind direction often results in an increased wind speed BIAS.
In general, this work demonstrates that, keeping restrictions and limits in mind, the mass consistent model can be a simple and useful tool to resolve the interaction of wind with small scale topography.

## Zusammenfassung

Die korrekte Darstellung von kleinskaligen Windfeldern, besonders über komplexer Topographie, stellt nach wie vor eine große Herausforderung dar. In dieser Arbeit wird ein massenkonsistentes Windmodell entwickelt. Als Vertikalkoordinate dient die terrain-folgende, auf Druck basierende $\eta$ Koordinate. Das Windmodell wird zuerst anhand einer idealisierten Simulation getestet und im Anschluss auf realen Daten angewendet. Als Eingabewindfeld dient eine 4 km WRF (Weather Research and Forecasting) Simulation. Dieses Windfeld wird auf ein 500 m Gitter mit genauerer Topographie interpoliert und mit Hilfe des massenkonsistenten Modells so angepasst, dass die Divergenz verschwindet. Um die Leistung des Modells zu quantifizieren, werden die Ergebnisse von vier Testfällen mit Bodenwetterbeobachtungen verglichen. Zusätzlich steht für den letzten Fall ein hochaufgelöstes Modell (1 km) zum Vergleich zur Verfügung. Um einen idealen Wert für den vertikalen Transmissionskoeffizienten $\alpha_\eta$ zu finden, der das Ergebnis maßgeblich beeinflusst, werden verschiedene empirische Werte verwendet. Außerdem wird der Wert von $\alpha_\eta$ in Abhängigkeit der Stabilität sowie der Standardabweichung des Eingabewindfeldes berechnet und die daraus resultierenden Windfelder analysiert.

Insgesamt ist die Leistung des massenkonsistenten Modells stark abhängig von der Qualität und Auflösung der Eingabedaten sowie den vorherrschenden Wetterbedingungen. Die besten Resultate werden tagsüber bei stabilen Verhältnissen und starkem synoptischen Forcing erreicht. Die Wiedergabe der Windrichtung kann im Vergleich mit dem 4 km-Modell am stärksten verbessert werden, mit einer Reduktion des RMS-Fehlers von bis zu 30°. Gleichzeitig kommt es jedoch meist zu einer Erhöhung des BIAS der Windgeschwindigkeit.
Generell zeigt diese Arbeit, dass das massenkonsistente Modell ein einfaches und sinnvolles Mittel sein kann um auf kleiner Skala die Interaktion von Wind und Topographie darzustellen sofern man gewisse Beschränkungen beachtet.

# Acknowledgements

First I would like to thank my supervisor Prof. Leopold Haimberger for his valuable input, feedback and advice on my thesis. I would also like to acknowledge UBIMET for the financial support and providing the data used in this work. Furthermore I would like to thank the employees of UBIMET, especially Dieter Mayer for sharing his ideas end expertise and to Manuel Safner with whom I spent several hours tracking down errors in my code.

Many thanks also go out to my sister for proofreading and to my friends for keeping up my motivation. Finally, I want to express my profound gratitude to my family for providing me with support and encouragement throughout the last years. This accomplishment would not have been possible without them.

# Contents

# Chapter 1

# Introduction

Since the beginning of operational weather forecast there has always been an aspiration towards better, more accurate forecasts. In the past 20 years the spatial resolution of global numerical weather models has been increased from 100 km down to 9 km thanks to ongoing research and development of supercomputers. Local weather models use the output of global models as boundary conditions to operate on even higher resolution to provide the most precise forecast possible. Nevertheless, due to the limited time for computations in operational services there are still restrictions regarding the temporal and spatial resolution of the models.

Amongst others, resolving small scale wind fields on high resolution topography (100 m to 1 km) still remains a challenging task. This work meets this challenge and focuses on producing accurate wind fields over complex terrain with a resolution of 500 m.

A solution to this problem can be used in many practical areas, including simulations of the spread of pollutants (Mayer et al. [2008], Cox et al. [1998]) or the selection and study of wind turbine sites [Phillips, 1979]. Research on finding a simple and fast way to compute wind fields over complex topography on a fine grid has been very active over the past decades and is still subject of modern-day investigations.

Over the years several types of models have been developed to address this problem. In general they can be divided into two categories, prognostic and diagnostic (steady state) flow models [Cox et al., 1998]. Prognostic models use a set of time dependent equations (conservation of mass, momentum, heat, water and other substances) to compute the evolution of atmospheric motion by integrating those equations over time and space. One can further differentiate between different types of prognostic models by the parameterization schemes used for phenomena that cannot be calculated directly or by the approximations made in the conservation equations (e.g. incompressible or hydrostatic) [Finardi et al., 1997]. The downside of using prognostic models is that the computation time increases rapidly when increasing temporal and spatial resolution. A popular and widely used example of a prognostic model is the WRF (Weather Research and Forecast) model, described in section (6.1).

Diagnostic models use equations that are not time dependent to calculate a steady state wind

field from a provided set of input data and can be further separated into two groups, linearized and mass consistent models. Linearized models, first introduced by Jackson and Hunt [1975], use linearized solutions of the Navier-Stokes equations to describe the boundary layer flow disturbed by terrain. The model divides the flow into an inner region where turbulence plays an important role, and an outer region where the flow is assumed to be inviscid [Finardi et al., 1997]. LINCOLM [Troen and De Baas, 1987] and WaSP [Mortensen et al., 2005] are just two examples out of many linearized models that have been developed and successfully used for reconstructing wind fields.

Mass consistent models use meteorological input data which can either be obtained from meteorological observations or from output from a numerical weather model. A three dimensional wind field is then created in two steps: Firstly, the input data is interpolated to the computational grid to generate an initial wind field. This wind field is then adjusted so that it fulfils mass conservation. Following Sasaki [1970], variational analysis is applied to find the non divergent wind field whilst making the smallest possible modifications to the initial field. Due to its simple physics, mass consistent models are relatively easy to handle and therefore widely used in applied problems. Furthermore, input data can be obtained easily and the computational cost is significantly lower compared to prognostic models for similar resolution.

However, the use of diagnostic models gives rise to some challenges and problems. The equation system that has to be solved contains factors, the Gaussian precision moduli or $\alpha$ constants, that have to be defined prior to the computations. These constants have to be found empirically and have major influence onto the final velocity field. The importance of the $\alpha$ constants is discussed in detail in section (4.3). Another disadvantage of using diagnostic models is the lack in prognostic capability. They cannot reproduce the full dynamics and small scale features of the atmosphere such as thermal effects or turbulent wakes unless they have already been represented in some form in the input data because they are based on a set of idealized equations.

In this work a mass consistent model was developed based on the theory of Sherman [1978]. The main purpose of this new diagnostic model is to downscale a wind field calculated by the prognostic numerical weather model (WRF model) from a 4 km grid to a finer grid with more detailed topographic information. In contrast to Magnusson [2005], a pressure based terrain following vertical coordinate, the $\eta$ coordinate, was chosen. This way, the model output of the WRF model which is used for operational forecast at UBIMET can be used directly as input data for the mass consistent model. This has the advantage that no coordinate transformations have to be performed prior to the computations and potential errors arising from such calculations can be avoided. Hence, this mass consistent model provides a tool to refine the model output in specific areas of interest and improve the quality of forecast of wind fields especially over complex terrain.

Regarding the $\alpha$ constants, different approaches have been made subsequently. Firstly different constant values for $\alpha$ are chosen and compared. Then the $\alpha$ constants are linked to the standard deviation of velocity components and atmospheric stability to compute the $\alpha$ constants automatically, depending on the weather condition.

To verify the accuracy and point out limitations of our model, four case studies representing four different weather conditions were conducted. The obtained results were compared to near-ground observations and radiosonde data. Innsbruck, a region in the west of Austria exhibiting highly interesting terrain, including high mountains and deep valleys, was chosen as a test region. A more detailed description of the area is given in section (6.2).

## 1.1 Previous Work

The first two models using the mass consistent approach were developed in the 1970s. MASCON [Dickerson, 1978], a mass consistent atmospheric flux model for regions with complex terrain, was used for air pollution modelling in the San Francisco Bay Area. The model treats the well mixed layer below the inversion as a single layer and uses mass consistent input data obtained from measurements of inversion base heights above topography and mean wind as input data. The product of these two sets of input data is adjusted by the MASCON algorithm so that air mass is conserved and the changes to the observational data are minimal.

Almost at the same time MATHEW, a mass-adjusted, three-dimensional wind field model, was developed by Sherman [1978], providing a pollutant transport model with input data. MATHEW produces a minimally adjusted windfield from observational wind-field data, interpolated and extrapolated to a computational grid. The vertical wind profile is calculated using a power law and the geostrophic wind from synoptic analysis as an upper boundary wind. Since all available field data was used as input, MATHEW has not been verified independently.

Two additional mass consistent models, NOABL [Phillips, 1979] and COMPLEX (Bhumralkar et al. [1980] and Endlich et al. [1982]) were tested and compared by Guo and Palutikof [1990] in three different regions within the UK. While COMPLEX was initially developed to investigate wind energy potential at a potential turbine site, NOABL was used to determine the spatial distribution of wind speed and direction from observational data. Both models use terrain following coordinates and require measurements as input data. As an additional parameter the boundary layer height has to be specified. Both models performed well during the testing for neutrally stratified conditions with strong winds but had its difficulties with very steep topography where unrealistic streaming patterns were observed. The observed difference between calculated results and measurements at selected stations was 5 % at stations at lower altitude with wind speeds being too low, and 20 % at higher elevated stations for which the simulations showed higher wind speeds. Based on these findings, a new model, MC-3, has been developed which takes into account the anemometer height and roughness at different stations prior to interpolation to counteract the systematic over- and underestimation of wind speeds.

NUATMOS, a mass consistent model developed by Ross and Smith [1988] and based on ATMOS1 [Davis et al., 1984], has been tested in idealized simulations and compared with potential flow solutions. An attempt to couple the parameter that controls the amount of adjustment made in the horizontal and vertical direction with the Froude number to consider atmospheric stability

effects was made. The model was capable of reproducing the flow predicted by theory and any differences were attributed to boundary effects and resolution.

Cox et al. [1998] investigated the performance of a model called MINERVE, initially developed by Geai [1987], using meteorological measurements collected during April and December 1995 at White Sands Missile Range, New Mexico. MINERVE has been tested extensively prior to this work and was shown to describe the observed wind flow within 20 %. In most cases the wind fields provided by the model were consistent with observations. However, under some conditions like the breakup of an inversion, the difference between observed and modelled wind field was up to 60 %, pointing out the limits of this diagnostic model.

Further models based on the idea of mass consistency include CONDOR [Moussiopoulos et al., 1988], WINDS [Ratto et al., 1990] and WOCSS [Ludwig et al., 1991] but a detailed description is beyond the scope of this work.

# Chapter 2

# Derivation of the Mass Consistent Model

Since numerical high resolution models require a lot of computational power and time which often cannot be provided in operational forecast, a faster and less complex approach is required to find a more appropriate wind field on a high resolution topography.

The aim of this work is to find a wind field that is not only mass consistent at every grid point but also minimizes the variance between the original and the adjusted field. This should then represent the most reasonable solution because it also is the solution closest to the input field. Terrain following coordinates are used in order to simplify the boundary conditions especially when dealing with complex terrain [Magnusson, 2005].

In this section the theory behind the mass consistent model is described. The Euler-Lagrange equations for solving the problem are derived, first in pressure coordinates and then transformed to pressure based terrain following hybrid coordinates ($\eta$ coordinates), following the approach presented by Mayer and Wind [2015]. The derivation of this diagnostic model is based on variational analysis, a very powerful and widely applicable mathematical technique.

## 2.1 Calculus of Variation

This chapter gives a short overview on the principles of the Calculus of Variation and largely follows chapter 22 of Arfken and Weber [2013].

In general, Calculus of Variation describes a functional which has to be minimized (or maximized). The functional itself depends not just on variables but on functions. As a simple example, Arfken and Weber [2013] define an integral $J$ as a functional of $y$ as

$$J[y] = \int_{x_1}^{x_2} f\left(y(x), \frac{\mathrm{d}y(x)}{\mathrm{d}x}, x\right) \mathrm{d}x \tag{2.1}$$

where $f$ is a function of $y$, $\mathrm{d}y/\mathrm{d}x$ and $x$ with fixed limits. Subsequently, a variation $\delta y$ of the function $y$, a scale factor $\varepsilon$ that describes the magnitude of this variation and an arbitrary function $y'(x)$ with fixed endpoints are introduced:

$$y'(x_1) = y'(x_2) = 0. \tag{2.2}$$

Then $y$ can be written as a function of $x$ and $y'$ with

$$y(x, \varepsilon) = y(x, 0) + \varepsilon y'(x) \tag{2.3}$$

where $y(x.0)$ is chosen to minimize $J$. Using this equation, the integral (2.1) becomes

$$J(\varepsilon) = \int_{x_1}^{x_2} f\left(y(x,\varepsilon), \frac{\mathrm{d}y(x,\varepsilon)}{\mathrm{d}x}, x\right) \mathrm{d}x. \tag{2.4}$$

To obtain a stationary value for $J$ we can impose the following condition

$$\left.\frac{\partial J(\varepsilon)}{\partial \varepsilon}\right|_{\varepsilon=0} = 0. \tag{2.5}$$

Since the dependence on $\varepsilon$ in the integral is contained in $y(x, \varepsilon)$ and with the definition $\partial y(x,\varepsilon)/\partial x = \dot{y}$, the derivative of $J$ is

$$\frac{\partial J(\varepsilon)}{\partial \varepsilon} = \int_{x_1}^{x_2} \left[\frac{\partial f}{\partial y}\frac{\partial y}{\partial \varepsilon} + \frac{\partial f}{\partial \dot{y}}\frac{\partial \dot{y}}{\partial \varepsilon}\right] \mathrm{d}x = \int_{x_1}^{x_2} \left(\frac{\partial f}{\partial y} y'(x) + \frac{\partial f}{\partial \dot{y}}\frac{\mathrm{d}y'(x)}{\mathrm{d}x}\right) \mathrm{d}x = 0. \tag{2.6}$$

Integrating the second term of the integral and using equation (2.2) leads to

$$\frac{\partial J(\varepsilon)}{\partial \varepsilon} = \int_{x_1}^{x_2} \left[\frac{\partial f}{\partial y} - \frac{\mathrm{d}}{\mathrm{d}x}\frac{\partial f}{\partial \dot{y}}\right] y'(x)\mathrm{d}x = 0. \tag{2.7}$$

This equation can only be satisfied for arbitrary $y'(x)$ if the equation within the square brackets is equal to zero, yielding in a partial differential equation known as the Euler equation:

$$\frac{\partial f}{\partial y} - \frac{\mathrm{d}}{\mathrm{d}x}\frac{\partial f}{\partial \dot{y}} = 0 \tag{2.8}$$

For more than one $(n)$ unknown functions this theory can still be easily applied and results in a set of $n$ Euler equations:

$$\frac{\partial f}{\partial y_i} - \frac{\mathrm{d}}{\mathrm{d}x}\frac{\partial f}{\partial \dot{y}_i} = 0, \qquad i = 1, 2, \ldots, n \tag{2.9}$$

### 2.1.1 Constrained Minima

The (in this example three-dimensional) function $f(x, y, z)$ is now subject to the constraint $g(x, y, z) = C$, where $C$ is a constant. This problem corresponds to minimizing the function $f$ on a surface of a constant value $g$. To solve these constraint equations, the method of Lagrangian

multipliers $\lambda$ is introduced. For $n$ variables and $k$ constraints the equation is of the form

$$\frac{\partial f}{\partial x_i} - \sum_{j=1}^{k} \lambda_j \frac{\partial g_j}{\partial x_i} = 0, \qquad i = 1, 2, \ldots, n. \tag{2.10}$$

These $n$ equations, together with the $k$ constraint equations, represent the system of equations that has to be solved.

## 2.2 Derivation in Pressure Coordinates

In 1958 Sasaki introduced a formalism based on the Calculus of Variation, forming the basis for mass consistent models. The idea behind this method is to define an integral function whose minimal solution also minimizes the variance of the difference between the input values and the adjusted variables. In addition to minimizing the variance, a subsidiary physical constraint is defined which has to be satisfied exactly (strong constraint) or approximately (weak constraint) by the adjusted variables. In this model the three dimensional continuity equation

$$\boldsymbol{\nabla} \cdot v = \frac{\partial u}{\partial x} + \frac{\partial v}{\partial y} + \frac{\partial \omega}{\partial p} = 0 \tag{2.11}$$

is used as a strong constraint [Sherman, 1978]. Therefore the divergence of the adjusted wind field has to be zero at every grid point. The basic integral can be written as

$$\int_V \left[ \alpha_x^2 (u - u_0)^2 + \alpha_y^2 (v - v_0)^2 + \alpha_p^2 (\omega - \omega_0)^2 + 2\lambda \left( \frac{\partial u}{\partial x} + \frac{\partial v}{\partial y} + \frac{\partial \omega}{\partial p} \right) \right] \mathrm{d}V = \mathrm{Min} \tag{2.12}$$

where $\vec{v_0}(x, y, p) = [u_0, v_0, \omega_0]$ is the input field, $\vec{v}(x, y, p) = [u, v, \omega]$ is the adjusted field, $\alpha_i$ are the Gaussian precision moduli which have to be found empirically and $\lambda(x, y, p)$ is the Lagrange multiplier. A factor two is inserted to simplify further calculations.
The integral over the volume equals the integral over the three coordinates:

$$V = \int \mathrm{d}V = \iiint \mathrm{d}x\mathrm{d}y\mathrm{d}z. \tag{2.13}$$

The wind components $u$, $v$ and $\omega$ are assumed to minimize the integral in equation (2.12). To obtain the Euler-Lagrange differential equations for $\lambda$ auxiliary functions $\tilde{u}(x, y, p, \varepsilon)$, $\tilde{v}(x, y, p, \varepsilon)$ and $\tilde{\omega}(x, y, p, \varepsilon)$ are introduced. These functions split the velocity field in two parts, one being the field that minimizes the integral and the other one describing weighted variations of these velocity fields. The original fields are related to these functions as follows:

$$\tilde{u}(x, y, p, \varepsilon) = u(x, y, p) + \varepsilon u'(x, y, p) \tag{2.14}$$

$$\tilde{v}(x, y, p, \varepsilon) = v(x, y, p) + \varepsilon v'(x, y, p) \tag{2.15}$$

$$\tilde{\omega}(x, y, p, \varepsilon) = \omega(x, y, p) + \varepsilon \omega'(x, y, p). \tag{2.16}$$

The partial derivatives of the functions can be written as

$$\frac{\partial}{\partial x}\tilde{u}(x,y,p,\varepsilon) = \tfrac{\partial}{\partial x}u(x,y,p) + \varepsilon\tfrac{\partial}{\partial x}u'(x,y,p) \tag{2.17}$$

$$\frac{\partial}{\partial y}\tilde{v}(x,y,p,\varepsilon) = \tfrac{\partial}{\partial y}v(x,y,p) + \varepsilon\tfrac{\partial}{\partial y}v'(x,y,p) \tag{2.18}$$

$$\frac{\partial}{\partial p}\tilde{\omega}(x,y,p,\varepsilon) = \tfrac{\partial}{\partial p}\omega(x,y,p) + \varepsilon\tfrac{\partial}{\partial p}\omega'(x,y,p). \tag{2.19}$$

The variations $u'$, $v'$ and $\omega'$ are arbitrary and have to be zero at the boundaries, the weight factor $\varepsilon$ is defined to be small $[0 < \varepsilon \ll 1]$. The integral (2.12) for the variations is defined as

$$\tilde{I} = \int \left[\alpha_x^2\,(\tilde{u}-u_0)^2 + 2\,\lambda\frac{\partial\tilde{u}}{\partial x} + \alpha_y^2\,(\tilde{v}-v_0)^2 + 2\,\lambda\frac{\partial\tilde{v}}{\partial y} + \alpha_p^2\,(\tilde{\omega}-\omega_0)^2 + 2\,\lambda\frac{\partial\tilde{\omega}}{\partial p}\right]\mathrm{d}V = \mathrm{Min.} \tag{2.20}$$

After plugging in the functions (2.14)-(2.16) the integral can be expressed as

$$\begin{aligned}\tilde{I} &= \int \Big[\alpha_x^2\left(u+\varepsilon\,u'-u_0\right)^2 + 2\lambda\frac{\partial}{\partial x}(u+\varepsilon\,u') + \alpha_y^2\left(v+\varepsilon\,v'-v_0\right)^2 + \\ &+ 2\lambda\frac{\partial}{\partial y}(v+\varepsilon\,v') + \alpha_p^2\left(\omega+\varepsilon\,\omega'-\omega_0\right)^2 + 2\lambda\frac{\partial}{\partial p}\left(\omega+\varepsilon\,\omega'\right)\Big]\mathrm{d}V.\end{aligned} \tag{2.21}$$

If $\varepsilon$ is zero, the original values $u$, $v$ and $\omega$ minimize the integral (2.21). Hence the relationship

$$\left.\frac{\mathrm{d}\tilde{I}}{\mathrm{d}\varepsilon}\right|_{\varepsilon=0} = 0 \tag{2.22}$$

is valid. For the total derivative with respect to $\varepsilon$, the chain rule has to be applied:

$$\frac{\mathrm{d}}{\mathrm{d}\varepsilon} = \frac{\partial}{\partial\tilde{u}}\frac{\partial\tilde{u}}{\partial\varepsilon} + \frac{\partial}{\partial\tilde{v}}\frac{\partial\tilde{v}}{\partial\varepsilon} + \frac{\partial}{\partial\tilde{\omega}}\frac{\partial\tilde{\omega}}{\partial\varepsilon} + \frac{\partial}{\partial\left(\frac{\partial\tilde{u}}{\partial x}\right)}\frac{\partial\left(\frac{\partial\tilde{u}}{\partial x}\right)}{\partial\varepsilon} + \frac{\partial}{\partial\left(\frac{\partial\tilde{v}}{\partial y}\right)}\frac{\partial\left(\frac{\partial\tilde{v}}{\partial y}\right)}{\partial\varepsilon} + \frac{\partial}{\partial\left(\frac{\partial\tilde{\omega}}{\partial p}\right)}\frac{\partial\left(\frac{\partial\tilde{\omega}}{\partial p}\right)}{\partial\varepsilon}. \tag{2.23}$$

Applying equation (2.23) to integral (2.21) gives:

$$\left.\frac{\partial\tilde{I}}{\partial\tilde{u}}\frac{\partial\tilde{u}}{\partial\tilde{\varepsilon}}\right|_{\varepsilon=0} = \int\left[2\,\alpha_x^2\,(\tilde{u}-u_0)\,u'\big|_\varepsilon\right]\mathrm{d}V = \int\left[2\,\alpha_x^2\,(u-u_0)\,u'\big|_\varepsilon\right]\mathrm{d}V \tag{2.24}$$

$$\left.\frac{\partial\tilde{I}}{\partial\tilde{v}}\frac{\partial\tilde{v}}{\partial\tilde{\varepsilon}}\right|_{\varepsilon=0} = \int\left[2\,\alpha_y^2\,(\tilde{v}-v_0)\,v'\big|_\varepsilon\right]\mathrm{d}V = \int\left[2\,\alpha_y^2\,(v-v_0)\,v'\big|_\varepsilon\right]\mathrm{d}V \tag{2.25}$$

$$\left.\frac{\partial\tilde{I}}{\partial\tilde{\omega}}\frac{\partial\tilde{\omega}}{\partial\tilde{\varepsilon}}\right|_{\varepsilon=0} = \int\left[2\,\alpha_p^2\,(\tilde{\omega}-\omega_0)\,\omega'\big|_\varepsilon\right]\mathrm{d}V = \int\left[2\,\alpha_p^2\,(\omega-\omega_0)\,\omega'\big|_\varepsilon\right]\mathrm{d}V \tag{2.26}$$

$$\left.\frac{\partial\tilde{I}}{\partial\left(\frac{\partial\tilde{u}}{\partial x}\right)}\frac{\partial\left(\frac{\partial\tilde{u}}{\partial x}\right)}{\partial\varepsilon}\right|_{\varepsilon=0} = \int\left[2\lambda\left.\frac{\partial\frac{\partial\tilde{u}}{\partial x}}{\partial\varepsilon}\right|_{\varepsilon=0}\right]\mathrm{d}V = \int\left[2\lambda\frac{\partial u'}{\partial x}\right]\mathrm{d}V \tag{2.27}$$

$$\left.\frac{\partial\tilde{I}}{\partial\left(\frac{\partial\tilde{v}}{\partial y}\right)}\frac{\partial\left(\frac{\partial\tilde{v}}{\partial y}\right)}{\partial\varepsilon}\right|_{\varepsilon=0} = \int\left[2\lambda\left.\frac{\partial\frac{\partial\tilde{v}}{\partial y}}{\partial\varepsilon}\right|_{\varepsilon=0}\right]\mathrm{d}V = \int\left[2\lambda\frac{\partial v'}{\partial y}\right]\mathrm{d}V \tag{2.28}$$

$$\left.\frac{\partial \tilde{I}}{\partial\left(\frac{\partial\tilde{\omega}}{\partial p}\right)}\frac{\partial\left(\frac{\partial\tilde{\omega}}{\partial p}\right)}{\partial\varepsilon}\right|_{\varepsilon=0} = \int\left[2\lambda\left.\frac{\partial\frac{\partial\tilde{\omega}}{\partial p}}{\partial\varepsilon}\right|_{\varepsilon=0}\right]\mathrm{d}V = \int\left[2\lambda\frac{\partial\omega'}{\partial p}\right]\mathrm{d}V. \tag{2.29}$$

Using partial integration and the condition that the variations $u'$, $v'$ and $\omega'$ vanish at the boundaries of the integral, equations (2.27), (2.28) and (2.29) can be simplified:

$$\int_{p_1}^{p_2}\int_{y_1}^{y_2}\left\{\int_{x_1}^{x_2}\left[2\lambda\frac{\partial u'}{\partial x}\right]\mathrm{d}x\right\}\mathrm{d}y\,\mathrm{d}p = \int_{p_1}^{p_2}\int_{y_1}^{y_2}\left\{\underbrace{2\lambda\,u'\big|_{x_1}^{x_2}}_{=0} - \int_{x_1}^{x_2}2\,\frac{\partial\lambda}{\partial x}u'\,\mathrm{d}x\right\}\mathrm{d}y\,\mathrm{d}p = -\int 2\,\frac{\partial\lambda}{\partial x}\,u'\,\mathrm{d}V \tag{2.30}$$

$$\int_{x_1}^{x_2}\int_{p_1}^{p_2}\left\{\int_{y_1}^{y_2}\left[2\lambda\frac{\partial v'}{\partial y}\right]\mathrm{d}y\right\}\mathrm{d}x\,\mathrm{d}p = \int_{x_1}^{x_2}\int_{p_1}^{p_2}\left\{\underbrace{2\lambda\,v'\big|_{y_1}^{y_2}}_{=0} - \int_{y_1}^{y_2}2\,\frac{\partial\lambda}{\partial y}v'\,\mathrm{d}y\right\}\mathrm{d}x\,\mathrm{d}p = -\int 2\,\frac{\partial\lambda}{\partial y}\,v'\,\mathrm{d}V \tag{2.31}$$

$$\int_{x_1}^{x_2}\int_{y_1}^{y_2}\left\{\int_{p_1}^{p_2}\left[2\lambda\frac{\partial\omega'}{\partial p}\right]\mathrm{d}p\right\}\mathrm{d}x\,\mathrm{d}y = \int_{x_1}^{x_2}\int_{y_1}^{y_2}\left\{\underbrace{2\lambda\,\omega'\big|_{p_1}^{p_2}}_{=0} - \int_{p_1}^{p_2}2\,\frac{\partial\lambda}{\partial p}\omega'\,\mathrm{d}p\right\}\mathrm{d}x\,\mathrm{d}y = -\int 2\,\frac{\partial\lambda}{\partial p}\,\omega'\,\mathrm{d}V \tag{2.32}$$

Summarizing all terms and inserting them into equation (2.22) gives rise to the following relationship:

$$\left.\frac{\mathrm{d}\tilde{I}}{\mathrm{d}\varepsilon}\right|_{\varepsilon=0} = 2\int\left\{\left[\alpha_x^2\,(u-u_0) - \frac{\partial\lambda}{\partial x}\right]u' + \left[\alpha_y^2\,(v-v_0) - \frac{\partial\lambda}{\partial y}\right]v' + \left[\alpha_p^2\,(\omega-\omega_0) - \frac{\partial\lambda}{\partial p}\right]\omega'\right\}\mathrm{d}V = 0. \tag{2.33}$$

Since the variations $u'$, $v'$ and $\omega'$ are arbitrary the integral above can only vanish if the corresponding values in the square brackets in front of the variations are zero. This leads to the following equations:

$$\alpha_x^2\,(u-u_0) - \frac{\partial\lambda}{\partial x} = 0 \quad\Rightarrow\quad u = u_0 + \frac{1}{\alpha_x^2}\frac{\partial\lambda}{\partial x} \tag{2.34}$$

$$\alpha_y^2\,(v-v_0) - \frac{\partial\lambda}{\partial y} = 0 \quad\Rightarrow\quad v = v_0 + \frac{1}{\alpha_y^2}\frac{\partial\lambda}{\partial y} \tag{2.35}$$

$$\alpha_p^2\,(\omega-\omega_0) - \frac{\partial\lambda}{\partial p} = 0 \quad\Rightarrow\quad \omega = \omega_0 + \frac{1}{\alpha_p^2}\frac{\partial\lambda}{\partial p}. \tag{2.36}$$

Together with the continuity equation (2.11) we now have four equations for four unknown variables ($u$, $v$, $\omega$, $\lambda$) which closes the system of equations.

### 2.2.1 Differential Equation for the Lagrange Multiplier $\lambda$

To obtain the differential equation for $\lambda$, equations (2.34), (2.35) and (2.36) have to be plugged in to the continuity equation (2.11):

$$\frac{\partial u_0}{\partial x} + \frac{1}{\alpha_x^2}\frac{\partial^2\lambda}{\partial x^2} + \frac{\partial v_0}{\partial y} + \frac{1}{\alpha_y^2}\frac{\partial^2\lambda}{\partial y^2} + \frac{\partial\omega_0}{\partial p} + \frac{1}{\alpha_p^2}\frac{\partial^2\lambda}{\partial p^2} = 0. \tag{2.37}$$

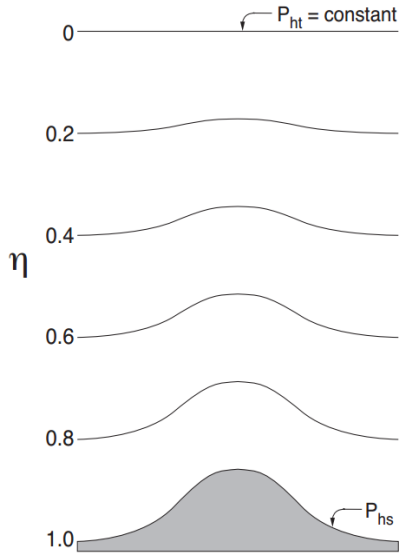


**Figure 2.1:** The vertical $\eta$ coordinate. $p_{hs}$ and $p_{ht}$ correspond to the pressure values at the surface and the top boundaries [Skamarock et al., 2008].

Rearranging the terms leads to a partial differential equation second order for the Lagrange multiplier:

$$\frac{1}{\alpha_x^2}\frac{\partial^2\lambda}{\partial x^2} + \frac{1}{\alpha_y^2}\frac{\partial^2\lambda}{\partial y^2} + \frac{1}{\alpha_p^2}\frac{\partial^2\lambda}{\partial p^2} = -\left[\frac{\partial u_0}{\partial x} + \frac{\partial v_0}{\partial y} + \frac{\partial \omega_0}{\partial p}\right]. \tag{2.38}$$

The right side represents the divergence of the input wind field which is usually available on some defined grid can be computed. Thus the only unknown variable in equation (2.38) is $\lambda$. This equation is solved numerically. The discretization that will be introduced in chapter 3, is carried out using terrain following coordinates.

## 2.3 The Terrain Following $\eta$ Coordinate

Although using the geometrical height as a vertical coordinate seems to be the most obvious and simple idea, the height coordinate system is not used in hydrostatic numerical weather models. The use of pressure coordinates brings the advantage of reducing the mass continuity equation to a diagnostic equation but at the same time introduces certain computational disadvantages in mountainous terrain where the lower boundary does not coincide with the coordinate surface [Kasahara, 1974]. Therefore, a variety of terrain following coordinates have been developed over the past few decades.

The vertical coordinate used in the WRF model (described in section 6.1) is the $\eta$ coordinate, whose output is used for further computations in this thesis. The $\eta$ coordinate is defined by

$$\eta(x, y, p) = \frac{p(x, y) - p_t}{p_s(x, y) - p_t} \tag{2.39}$$

where $p(x, y)$ is pressure at the corresponding grid point, $p_t$ is pressure at the top of the domain and $p_s(x, y)$ is surface pressure [Laprise, 1992]. Using this definition, the $\eta$ coordinate is a minor generalisation of the $\sigma$ coordinate $p/p_s$ which first was introduced by Phillips [1957].The value of $\eta$ varies between 1 on the surface ($p = p_s$) and 0 at the top ($p = p_t$)(see figure 2.1). On transformation between pressure and $\eta$ coordinates, the horizontal coordinates $x$ and $y$ remain the same while the vertical coordinate and thus the vertical velocity has to be adapted:

$$x \Rightarrow x \qquad u \Rightarrow u^* = u \tag{2.40}$$

$$y \Rightarrow y \qquad v \Rightarrow v^* = v \tag{2.41}$$

$$p \Rightarrow \eta \qquad \omega = \mathrm{d}p/\mathrm{d}t \Rightarrow \omega^* = \mathrm{d}\eta/\mathrm{d}t. \tag{2.42}$$

To find an equation for the vertical velocity, the coordinate $\eta$ which is a function of $p(t)$ and $p_s(x(t), y(t))$ has to be differentiated with respect to $t$:

$$\omega^* = \frac{\mathrm{d}\eta}{\mathrm{d}t} = \frac{\partial\eta}{\partial p}\underbrace{\frac{\mathrm{d}p}{\mathrm{d}t}}_{\omega} + \frac{\partial\eta}{\partial p_s}\frac{\partial p_s}{\partial x}\underbrace{\frac{\mathrm{d}x}{\mathrm{d}t}}_{u} + \frac{\partial\eta}{\partial p_s}\frac{\partial p_s}{\partial y}\underbrace{\frac{\mathrm{d}y}{\mathrm{d}t}}_{v} \tag{2.43}$$

The partial derivatives from equation (2.43) are then calculated separately:

$$\frac{\partial\eta}{\partial p} = \frac{1}{p_s(x, y) - p_t} \tag{2.44}$$

$$\frac{\partial\eta}{\partial p_s} = -\frac{p(x, y) - p_t}{(p_s(x, y) - p_t)^2}. \tag{2.45}$$

To replace $p(x, y)$ in equation (2.45), equation (2.39) can be resolved for $p$

$$p(x, y) = \eta(x, y, p)\ (p_s(x, y) - p_t) + p_t \tag{2.46}$$

and inserted into equation (2.45):

$$\frac{\partial\eta}{\partial p_s} == -\frac{\eta\ (p_s(x, y) - p_t) + p_t - p_t}{(p_s(x, y) - p_t)^2} = -\frac{\eta}{p_s(x, y) - p_t}. \tag{2.47}$$

Plugging equations (2.44) and (2.47) into equation (2.43) yields

$$\omega^* = -\frac{\eta}{p_s - p_t}\frac{\partial p_s}{\partial x}\,u - \frac{\eta}{p_s - p_t}\frac{\partial p_s}{\partial y}\,v + \frac{1}{p_s - p_t}\,\omega. \tag{2.48}$$

Taking a closer look at this equation, one can see that the horizontal surface pressure gradients $\partial p_s/\partial x$ and $\partial p_s/\partial x$ can induce a vertical velocity in $\eta$ coordinates even when the initial vertical velocity in $p$ coordinates is zero. The influence of the pressure gradients, which corresponds to the influence of the topography, on $\omega^*$ decreases while the influence of the last term in equation (2.48) increases with height.

## 2.4 Transformation of the Continuity Equation

The continuity equation in generalized coordinates $q_j$ is of the form

$$\frac{\dot{\rho}}{\rho} + \frac{\partial \dot{q}_j}{\partial q_j} + \frac{\dot{D}_q^x}{D_q^x} = 0 \tag{2.49}$$

where $\rho$ is the density, $D_q^x$ the Jacobian and the dotted values denote time derivatives [Hantel, 2013]. Starting in pressure coordinates and transforming to $\eta$ coordinates, the first term in equation (2.49) is zero. The Jacobian $D_\eta^p$ for this transformation can be calculated and has the form

$$D_\eta^p = \left| \begin{pmatrix} \frac{\partial x}{\partial x} & \frac{\partial x}{\partial y} & \frac{\partial x}{\partial \eta} \\ \frac{\partial y}{\partial x} & \frac{\partial y}{\partial y} & \frac{\partial y}{\partial \eta} \\ \frac{\partial p}{\partial x} & \frac{\partial p}{\partial y} & \frac{\partial p}{\partial \eta} \end{pmatrix} \right| = \left| \begin{pmatrix} 1 & 0 & \frac{\partial x}{\partial \eta} \\ 0 & 1 & \frac{\partial y}{\partial \eta} \\ 0 & 0 & p_s - p_t \end{pmatrix} \right| = p_s - p_t \tag{2.50}$$

where $\partial p / \partial \eta$ was derived from equation (2.46). The time derivative of the Jacobian is thus

$$\dot{D}_\eta^p(p_s(x(t), y(t))) = \frac{\partial \dot{D}_\eta^p}{\partial p_s} \frac{\partial p_s}{\partial x} \frac{\mathrm{d}x}{\mathrm{d}t} + \frac{\partial \dot{D}_\eta^p}{\partial p_s} \frac{\partial p_s}{\partial y} \frac{\mathrm{d}y}{\mathrm{d}t} = \frac{\partial p_s}{\partial x} u + \frac{\partial p_s}{\partial y} v. \tag{2.51}$$

Assembling the results of equations (2.50) and (2.51) and plugging it in into equation (2.49) yields the continuity equation in $\eta$ coordinates:

$$\frac{\partial u}{\partial x} + \frac{\partial v}{\partial y} + \frac{\partial \omega^*}{\partial \eta} + \frac{1}{p_s - p_t} \left[ \frac{\partial p_s}{\partial x} u + \frac{\partial p_s}{\partial y} v \right] = 0. \tag{2.52}$$

## 2.5 Eulerian Differential Equations in $\eta$ Coordinates

After deriving the vertical velocity and the continuity equation in $\eta$ cooridnates, the obtained additional terms have to be considered when minimizing integral (2.12). The new, extended integral has the form

$$\begin{aligned} \tilde{I} = \int \Big[ & \alpha_x^2 \left( \tilde{u} - u_0 \right)^2 + \alpha_y^2 \left( \tilde{v} - v_0 \right)^2 + \alpha_\eta^2 \left( \tilde{\omega}^* - \omega_0^* \right)^2 + \\ & + 2\lambda \left( \frac{\partial \tilde{u}}{\partial x} + \frac{\partial \tilde{v}}{\partial y} + \frac{\partial \tilde{\omega^*}}{\partial \eta} + \frac{1}{p_s - p_t} \left[ \frac{\partial p_s}{\partial x} \tilde{u} + \frac{\partial p_s}{\partial y} \tilde{v} \right] \right) \Big] \, \mathrm{d}V = \text{Min.} \end{aligned} \tag{2.53}$$

Following a similar procedure as described in section (2.2), the previously defined auxiliary functions (2.14-2.19) are reused for $u$, $v$ and $\omega^*$ and plugged into equation (2.53):

$$\begin{aligned} \tilde{I} \;=\; & \int \Big[ \alpha_x^2 \left( u + \varepsilon u' - u_0 \right)^2 + 2\lambda \left( \frac{\partial}{\partial x} \left( u + \varepsilon u' \right) + \frac{1}{p_s - p_t} \frac{\partial p_s}{\partial x} \left( u + \varepsilon u' \right) \right) + \\ & + \alpha_y^2 \left( v + \varepsilon v' - v_0 \right)^2 + 2\lambda \left( \frac{\partial}{\partial y} \left( v + \varepsilon v' \right) + \frac{1}{p_s - p_t} \frac{\partial p_s}{\partial y} \left( v + \varepsilon v' \right) \right) + \\ & + \alpha_\eta^2 \left( \omega^* + \varepsilon \omega^{*\prime} - \omega^*{}_0 \right)^2 + 2\lambda \left( \frac{\partial}{\partial \eta} \left( \omega^* + \varepsilon \omega^* \right) \right) \Big]. \end{aligned} \tag{2.54}$$

The partial derivatives of integral $\tilde{I}$ with respect to $\varepsilon$ at $\varepsilon = 0$ can now be written as

$$\left.\frac{\partial \tilde{I}}{\partial \tilde{u}}\frac{\partial \tilde{u}}{\partial \varepsilon}\right|_{\varepsilon=0} = \int \left[2\,\alpha_x^2\,(u-u_0)\,u' + \frac{2\,\lambda}{p_s-p_t}\left[\frac{\partial p_s}{\partial x}\right]u'\right]\mathrm{d}V \tag{2.55}$$

$$\left.\frac{\partial \tilde{I}}{\partial \tilde{v}}\frac{\partial \tilde{v}}{\partial \varepsilon}\right|_{\varepsilon=0} = \int \left[2\,\alpha_y^2\,(v-v_0)\,v' + \frac{2\,\lambda}{p_s-p_t}\left[\frac{\partial p_s}{\partial y}\right]v'\right]\mathrm{d}V \tag{2.56}$$

$$\left.\frac{\partial \tilde{I}}{\partial \tilde{\omega}^*}\frac{\partial \tilde{\omega}^*}{\partial \varepsilon}\right|_{\varepsilon=0} = \int \left[2\,\alpha_\eta^2\,(\omega^*-\omega_0^*)\,\omega^{*\prime}\right]\mathrm{d}V \tag{2.57}$$

$$\left.\frac{\partial \tilde{I}}{\partial\left(\frac{\partial \tilde{u}}{\partial x}\right)}\frac{\partial\left(\frac{\partial \tilde{u}}{\partial x}\right)}{\partial \varepsilon}\right|_{\varepsilon=0} = \int \left[2\lambda\frac{\partial u'}{\partial x}\right]\mathrm{d}V \tag{2.58}$$

$$\left.\frac{\partial \tilde{I}}{\partial\left(\frac{\partial \tilde{v}}{\partial y}\right)}\frac{\partial\left(\frac{\partial \tilde{v}}{\partial y}\right)}{\partial \varepsilon}\right|_{\varepsilon=0} = \int \left[2\lambda\frac{\partial v'}{\partial y}\right]\mathrm{d}V \tag{2.59}$$

$$\left.\frac{\partial \tilde{I}}{\partial\left(\frac{\partial \tilde{\omega^*}}{\partial \eta}\right)}\frac{\partial\left(\frac{\partial \tilde{\omega}^*}{\partial \eta}\right)}{\partial \varepsilon}\right|_{\varepsilon=0} = \int \left[2\lambda\frac{\partial \omega^{*\prime}}{\partial \eta}\right]\mathrm{d}V. \tag{2.60}$$

Equations (2.58)-(2.60) can be simplified using partial integration analogous to equations (2.30)-(2.32). Putting everything together results in the following equation:

$$\begin{aligned}\left.\frac{\mathrm{d}\tilde{I}}{\mathrm{d}\varepsilon}\right|_{\varepsilon=0} = 2\int\Bigg\{&\left[\alpha_x^2\,(u-u_0) - \frac{\partial\lambda}{\partial x} + \frac{\lambda}{p_s-p_t}\frac{\partial p_s}{\partial x}\right]u' + \\ &+ \left[\alpha_y^2\,(v-v_0) - \frac{\partial\lambda}{\partial y} + \frac{\lambda}{p_s-p_t}\frac{\partial p_s}{\partial y}\right]v' \\ &+ \left[\alpha_\eta^2\,(\omega*-\omega_0^*) - \frac{\partial\lambda}{\partial \eta}\right]\omega^{*\prime}\Bigg\}\mathrm{d}V = 0.\end{aligned} \tag{2.61}$$

The variations $u'$, $v'$ and $\omega'$ are independent and arbitrary. Hence the terms in the brackets in front of these variations have to disappear. Solving these terms for $u$, $v$ and $\omega^*$ results in:

$$u = u_0 + \frac{1}{\alpha_x^2}\left[\frac{\partial\lambda}{\partial x} - \frac{\lambda}{p_s-p_t}\frac{\partial p_s}{\partial x}\right] \tag{2.62}$$

$$y = y_0 + \frac{1}{\alpha_y^2}\left[\frac{\partial\lambda}{\partial y} - \frac{\lambda}{p_s-p_t}\frac{\partial p_s}{\partial y}\right] \tag{2.63}$$

$$\omega^* = {\omega_0}^* + \frac{1}{\alpha_\eta^2}\left[\frac{\partial\lambda}{\partial \eta}\right]. \tag{2.64}$$

With the subsequent abbreviations

$$Z_x = -\frac{1}{p_s-p_t}\frac{\partial p_s}{\partial x} \tag{2.65}$$

$$Z_y = -\frac{1}{p_s-p_t}\frac{\partial p_s}{\partial y} \tag{2.66}$$

equations (2.62) to (2.64) can be written as

$$u = u_0 + \frac{1}{\alpha_x^2}\left[\frac{\partial \lambda}{\partial x} + \lambda\, Z_x\right] \tag{2.67}$$

$$v = v_0 + \frac{1}{\alpha_y^2}\left[\frac{\partial \lambda}{\partial y} + \lambda\, Z_y\right] \tag{2.68}$$

$$\omega^* = {\omega_0}^* + \frac{1}{\alpha_\eta^2}\left[\frac{\partial \lambda}{\partial \eta}\right]. \tag{2.69}$$

### 2.5.1 Differential Equation for the Lagrange Multiplier $\lambda$

To obtain the final differential equation for the Lagrange multiplier $\lambda$, equations (2.67) to (2.69) have to be plugged into the continuity equation in $\eta$ coordinates (2.52):

$$\begin{aligned} \frac{1}{\alpha_x^2}\frac{\partial \lambda}{\partial x} + \frac{1}{\alpha_y^2}\frac{\partial \lambda}{\partial y} + \frac{1}{\alpha_\eta^2}\frac{\partial \lambda}{\partial \eta} \quad + \\ \frac{1}{\alpha_x^2}\lambda\frac{\partial Z_x}{\partial x} + \frac{1}{\alpha_y^2}\lambda\frac{\partial Z_y}{\partial y} - \frac{1}{\alpha_x^2}\lambda\, Z_x^2 - \frac{1}{\alpha_y^2}\lambda\, Z_y^2 \quad = \\ = -\left[\frac{\partial u_0}{\partial x} + \frac{\partial v_0}{\partial y} + \frac{\partial {\omega^*}_0}{\partial \eta} - Z_x\, u_0 - Z_y\, v_0\right]. \end{aligned} \tag{2.70}$$

The left hand side of the equation contains the terms with the Lagrange multiplier, the right hand side represents the divergence of the input wind field. Solving this equation numerically yields the Lagrange multiplier as a function of space ($\lambda(x, y, \eta)$) which can then be used to compute the new wind components by solving equations (2.67) to (2.69).

# Chapter 3

# Discretization

To obtain a solution to the continuous problem derived in the previous chapter equation 2.70 needs to be discretized and solved numerically. The formulation of the discretized equations is described in this chapter. Additionally section 3.2 discusses the choice of boundary conditions.

## 3.1 Discretizing the Continuous Equations

The equation to solve, equation (2.70), has the form $C_1\nabla^2\lambda + C_2\nabla\lambda + C_3\lambda = F$ with $C_i$ and $F$ being space-dependent scalar functions. Kapitza and Eppel [1987] define the discretization of the first and second derivatives of a function $\lambda$ with respect to the coordinate $x$ as

$$\frac{\partial\lambda}{\partial x} = \frac{\Delta_i^2\lambda_{i+1} - \left(\Delta_i^2 - \Delta_{i+1}^2\right)\lambda_i - \Delta_{i+1}^2\lambda_{i-1}}{\Delta_i\Delta_{i+1}\left(\Delta_i + \Delta_{i+1}\right)} \tag{3.1}$$

$$\frac{\partial^2\lambda}{\partial x^2} = \frac{2\left[\Delta_i\lambda_{i+1} - \left(\Delta_i - \Delta_{i+1}\right)\lambda_i - \Delta_{i+1}\lambda_{i-1}\right]}{\Delta_i\Delta_{i+1}\left(\Delta_i + \Delta_{i+1}\right)} \tag{3.2}$$

with grid distances $\Delta_i = x_i - x_{i-1}$ and $\Delta_{i+1} = x_{i+1} - x_i$. With this formulation the grid does not need to be equally spaced which, in our case, is true for the vertical coordinate. Applying equations (3.1) and (3.2) to equation (2.70) using indices $i$ and $j$ for the horizontal and $k$ for the vertical dimensions results in the following equation:

$$\begin{aligned}
& \frac{2}{\alpha_x^2}\left[\frac{\Delta_i\lambda_{i+1,j,k} - \left(\Delta_i + \Delta_{i+1}\right)\lambda_{i,j,k} + \Delta_{i+1}\lambda_{i-1,j,k}}{\Delta_i\,\Delta_{i+1}\left(\Delta_i + \Delta_{i+1}\right)}\right] \\
+ & \frac{2}{\alpha_y^2}\left[\frac{\Delta_j\lambda_{i,j+1,k} - \left(\Delta_j + \Delta_{j+1}\right)\lambda_{i,j,k} + \Delta_{j+1}\lambda_{i,j-1,k}}{\Delta_j\,\Delta_{j+1}\left(\Delta_j + \Delta_{j+1}\right)}\right] \\
+ & \frac{2}{\alpha_\eta^2}\left[\frac{\Delta_k\lambda_{i,j,k+1} - \left(\Delta_k + \Delta_{k+1}\right)\lambda_{i,j,k} + \Delta_{k+1}\lambda_{i,j,k-1}}{\Delta_k\,\Delta_{k+1}\left(\Delta_k + \Delta_{k+1}\right)}\right] \\
+ & \frac{\lambda_{i,j,k}}{\alpha_x^2}\left[\frac{\Delta_i^2\,Z_{x_{i+1,j}} - \left(\Delta_i^2 - \Delta_{i+1}^2\right)\,Z_{x_{i,j}} - \Delta_{i+1}^2\,Z_{x_{i-1,j}}}{\Delta_i\,\Delta_{i+1}\left(\Delta_i + \Delta_{i+1}\right)}\right]
\end{aligned}$$

$$
\begin{aligned}
&+ \quad \frac{\lambda_{i,j,k}}{\alpha_y^2}\left[\frac{\Delta_j^2\, Z_{y_{i,j+1}} - \left(\Delta_j^2 - \Delta_{j+1}^2\right)\, Z_{y_{i,j}} - \Delta_{j+1}^2\, Z_{y_{i,j-1}}}{\Delta_j\, \Delta_{j+1}\, (\Delta_j + \Delta_{j+1})}\right] \\
&- \quad \frac{1}{\alpha_x^2}\lambda_{i,j,k}\, Z_{x_{i,j}}^2 - \frac{1}{\alpha_y^2}\lambda_{i,j,k}\, Z_{y_{i,j}}^2 \\
= \quad &- \quad \frac{\Delta_i^2\, u_{0_{i+1,j,k}} - \left(\Delta_i^2 - \Delta_{i+1}^2\right)\, u_{0_{i,j,k}} - \Delta_{i+1}^2\, u_{0_{i-1,j,k}}}{\Delta_i\, \Delta_{i+1}\, (\Delta_i + \Delta_{i+1})} \\
&- \quad \frac{\Delta_j^2\, v_{0_{i,j+1,k}} - \left(\Delta_j^2 - \Delta_{j+1}^2\right)\, v_{0_{i,j,k}} - \Delta_{i+1}^2\, v_{0_{i,j-1,k}}}{\Delta_j\, \Delta_{j+1}\, (\Delta_j + \Delta_{j+1})} \\
&- \quad \frac{\Delta_k^2\, \omega^*_{0_{i,j,k+1}} - \left(\Delta_k^2 - \Delta_{k+1}^2\right)\, \omega^*_{0_{i,j,k}} - \Delta_{k+1}^2\, \omega^*_{0_{i,j,k-1}}}{\Delta_k\, \Delta_{k+1}\, (\Delta_k + \Delta_{k+1})} \\
&+ \quad Z_{x_{i,j}}\, u_{0_{i,j,k}} + Z_{y_{i,j}}\, v_{0_{i,j,k}}.
\end{aligned} \tag{3.3}
$$

Factoring out the Lagrange multipliers and taking into consideration that in our case the horizontal grid points are equally spaced, i.e. $\Delta_i = \Delta_{i+1} = \Delta_j = \Delta j + 1 \equiv \Delta$, simplifies equation (3.3) to

$$
\begin{aligned}
&\lambda_{i,j,k} \quad \left[-\frac{1}{\alpha_x^2}\left(\frac{2}{\Delta^2} + Z_{x_{i,j}}^2 - \frac{Z_{x_{i+1,j}} - Z_{x_{i-1,j}}}{2\Delta}\right)\right. \\
&\qquad \left. - \frac{1}{\alpha_y^2}\left(\frac{2}{\Delta^2} + Z_{y_{i,j}}^2 - \frac{Z_{y_{i,j+1}} - Z_{y_{i,j-1}}}{2\Delta}\right) - \frac{2}{\alpha_\eta^2 \Delta_k \Delta_{k+1}}\right] \\
&+ \quad \lambda_{i-1,j,k}\left[\frac{1}{\alpha_x^2\Delta^2}\right] + \lambda_{i+1,j,k}\left[\frac{1}{\alpha_x^2\Delta^2}\right] + \lambda_{i,j-1,k}\left[\frac{1}{\alpha_y^2\Delta^2}\right] + \lambda_{i,j+1,k}\left[\frac{1}{\alpha_y^2\Delta^2}\right] \\
&+ \quad \lambda_{i,j,k-1}\left[\frac{2}{\alpha_\eta^2\Delta_k(\Delta_k + \Delta_{k+1})}\right] + \lambda_{i,j,k+1}\left[\frac{2}{\alpha_\eta^2\Delta_{k+1}(\Delta_k + \Delta_{k+1})}\right] \\
= \quad &- \quad \left[\frac{u_{0_{i+1,j,k}} - u_{0_{i-1,j,k}}}{2\Delta}\right] - \left[\frac{v_{0_{i,j+1,k}} - v_{0_{i,j-1,k}}}{2\Delta}\right] + Z_{x_{i,j}}\, u_{0_{i,j,k}} + Z_{y_{i,j}} v_{0_{i,j,k}} \\
&- \quad \left[\frac{\Delta_k^2\omega^*_{0_{i,j,k+1}} - \left(\Delta_k^2 - \Delta_{k+1}^2\right)\omega^*_{0_{i,j,k}} - \Delta_{k+1}^2\omega^*_{0_{i,j,k-1}}}{\Delta_k\Delta_{k+1}\,(\Delta_k + \Delta_{k+1})}\right].
\end{aligned} \tag{3.4}
$$

The equation above can be put into the form of a matrix equation

$$
\mathcal{M}\lambda = r \tag{3.5}
$$

with $r$ representing the right hand side of equation (3.4). To find a solution to this equation, the indices $i, j, k$ are merged to one index $n$ where $n = 1, \ldots, n_i \cdot n_j \cdot n_k$. Consequently, the three-dimensional matrix of $\lambda$ becomes a vector and $\mathcal{M}$ becomes an $n \times n$ matrix. Furthermore, $\mathcal{M}$ only has 7 diagonals with non-zero elements and can therefore be treated as a sparse matrix, considerably reducing the computational cost.

## 3.2 Boundary Conditions

Using terrain following coordinates introduces a big advantage compared to cartesian coordinates considering boundary conditions when dealing with topography. Following Sherman [1978], either the adjustment of the velocity component normal to the boundary or $\lambda$ has to be zero. The resulting wind field can then be calculated using equations (2.67) to (2.69).

### Lateral and Upper Boundary

Setting $\lambda$ to zero at the boundary does not imply that the derivative of $\lambda$ normal to the boundary is zero. Therefore, the velocities can still be adjusted according to equations (2.67) to (2.69). This type of boundary condition is applied to the upper and lateral boundaries. These are so-called flow-through boundaries because an adjustments of the velocity component normal to the boundary also results in a change of mass flowing in or out of the volume.

### Lower Boundary

For the lower boundary a no-flow-through or closed boundary condition is applied in which the normal derivative of $\lambda$ is set to zero. Thus, no adjustment of the vertical wind component can be made. In combination with defining the wind components $u = v = \omega^* = 0$ no mass can enter or leave the volume through the lower boundary.

# Chapter 4

# The Mass Consistent Model

This chapter gives an overview on the main steps that have to be performed to correct the input wind data such that the new wind field is mass consistent. A flow chart that summarizes this process is shown in Figure 4.1. Additionally the role of the $\alpha$ constants is discussed in section 4.3.

## 4.1 Preparation of the Data

First of all, data has to be collected from the WRF model (cf. 6.1). This data comes on a 4 km horizontal grid and has 41 vertical levels. To reduce computational cost and time not all vertical levels are used for further computations, i.e. only the lowest six levels and every fifth level above. By maintaining the higher resolution in the lower levels the difference in the results are almost negligible. A more detailed discussion of the choice of vertical levels is given in chapter 7.

Once data has been collected from the numerical model, the desired area has to be cut out by specifying the starting- and endpoint in latitude and longitude. The area chosen for further computations is described in section 6.2. As a next step, to get a first guess for the high resolution wind field, the data has to be interpolated from the 4 km grid to the finer grid with a resolution of 500 m. A two dimensional linear interpolation scheme for interpolation on the hybrid planes is used.

It is important to note that the matter of interpolation is not trivial. A change in resolution on model surfaces also changes the vertical coordinate. As a consequence, horizontal gradients on model surfaces get modified by a non-linear term [Trenberth et al., 1993]. However, an ideal procedure for interpolating to higher resolution still has to be found.

## 4.2 Setting up the Equation System

Following the interpolation, several calculations have to be done to be able to compute the divergence of the input wind field which is the right hand side of the equation system (3.5).

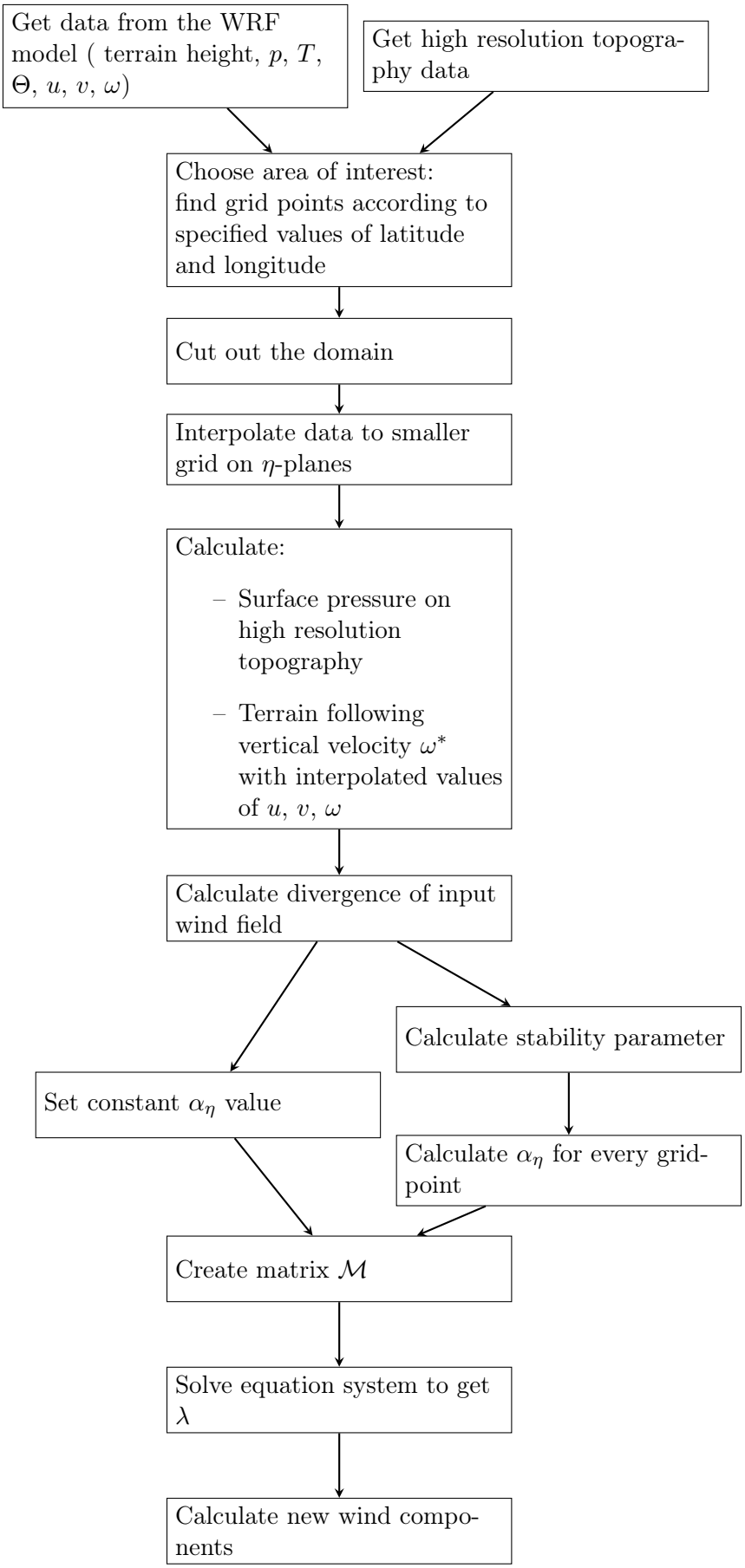


**Figure 4.1:** Steps of collecting and preparing data for the mass consistent model to compute the new wind field.

Firstly, the surface pressure on the high resolution topography is needed to obtain the horizontal pressure gradient. For this purpose the interpolated surface pressure $p_{s,i}$ is calculated from the interpolated terrain height $H_i$ on the corresponding high resolution terrain height $H$ at each grid point ($p_{s,new}$) using the barometric equation:

$$p_{s,new} = p_{s,i} \left( \frac{T_0}{T_0 + \Gamma \left( H_i - H \right)} \right)^{-\frac{g}{R\Gamma}}. \tag{4.1}$$

The following values of the standard atmosphere are assumed: $T_0 = 288.15\,\mathrm{K}$, the laps rate $\Gamma = -0.0065\,\mathrm{K\,m^{-1}}$, the ideal gas constant for dry air $R = 287.05\,\mathrm{J\,K^{-1}\,kg^{-1}}$ and the gravitational acceleration $g = 9.81\,\mathrm{m\,s^{-2}}$. With the new surface pressure $p_{s,new}$ the horizontal pressure gradients at each grid point $i, j$ can be calculated using centered differences:

$$\left( \frac{\partial p_s}{\partial x} \right)_{i,j} = \frac{p_{s_{i+1,j}} - p_{s_{i-1,j}}}{2\Delta x} \tag{4.2}$$

$$\left( \frac{\partial p_s}{\partial y} \right)_{i,j} = \frac{p_{s_{i,j+1}} - p_{s_{i,j-1}}}{2\Delta y} \tag{4.3}$$

At the lateral boundaries a one sided difference scheme of second order is used. $Z_x$ and $Z_y$ (equations 2.65 and 2.66) as well as the terrain following vertical velocity $\omega^*$ (equation 2.48) and subsequently the divergence of the input wind field can be computed using the right hand side of equation 3.4. The divergence is set to zero on the boundaries. Furthermore the resulting three dimensional matrix has to be rearranged to a vector.

As a next step the matrix $\mathcal{M}$ with dimensions $n \times n$ ($n = n_i \cdot n_j \cdot n_k$), where $i$ and $j$ are the horizontal and $k$ the vertical grid numbers, is created according to the left hand side of equation 3.4. As already mentioned in chapter 3 the matrix is sparsely populated with only 7 non-zero diagonals. The values $\neq 0$ which are the expressions within the brackets after the respective $\lambda$ in equation 3.4, with their corresponding indices can be seen in table 4.1. For the grid points at

| Variable | Value | Index |
|---|---|---|
| $\lambda_{i,j,k}$ | $-\frac{1}{\alpha_x^2}\left(\frac{2}{\Delta^2} + Z_{xi,j}^2 - \frac{Z_{xi+1,j} - Z_{xi-1,j}}{2\,\Delta}\right)$ $-\frac{1}{\alpha_y^2}\left(\frac{2}{\Delta^2} + Z_{yi,j}^2 - \frac{Z_{yi,j+1} - Z_{yi,j-1}}{2\,\Delta}\right) - \frac{2}{\alpha_z^2\,\Delta_k\,\Delta_{k+1}}$ | $n\ ,\ n$ |
| $\lambda_{i,j,k-1}$ | $\frac{2}{\alpha_z^2\,\Delta_k(\Delta_k + \Delta_{k+1})}$ | $n\ ,\ n-1$ |
| $\lambda_{i,j,k+1}$ | $\frac{2}{\alpha_z^2\,\Delta_{k+1}(\Delta_k + \Delta_{k+1})}$ | $n\ ,\ n+1$ |
| $\lambda_{i,j-1,k}$ | $\frac{1}{\alpha_y^2\,\Delta^2}$ | $n\ ,\ n-n_z$ |
| $\lambda_{i,j+1,k}$ | $\frac{1}{\alpha_y^2\,\Delta^2}$ | $n\ ,\ n+n_z$ |
| $\lambda_{i-1,j,k}$ | $\frac{1}{\alpha_x^2\,\Delta^2}$ | $n\ ,\ n-n_y n_z$ |
| $\lambda_{i+1,j,k}$ | $\frac{1}{\alpha_x^2\,\Delta^2}$ | $n\ ,\ n+n_y n_z$ |

**Table 4.1:** Non-zero elements of the matrix $\mathcal{M}$ with their corresponding variable and index.

the lateral boundaries ($i = j = 1$ and $i = n_x$, $j = n_y$) the value in the main diagonal is set to 1. Concerning the points at the lower boundary ($k = 1$), the main diagonal values are filled with $-1$ and the values to the right of the diagonal (index $n, n + 1$) with 1.

The equation system $\mathcal{M}\lambda = r$ can now be solved for $\lambda$ using LDL decomposition. The resulting vector contains the $\lambda$ values for every grid point and has to be rearranged into a three dimensional matrix. Finally the new wind field can be calculated with equations 2.67 to 2.69. The horizontal and vertical gradients of $\lambda$ used in these equations are calculated analogous to equations 4.2 and 4.3.

## 4.3 The $\alpha$ Constants

The choice of the Gaussian precision moduli ($\alpha$ constants) has major influence on the resulting wind field. They can be interpreted as weighting factors that define the relative amount of adjustment of the vertical and horizontal velocity components in the solution of the continuity equation [Finardi et al., 1997]. The ratio between horizontal $\alpha_h$ and vertical $\alpha_v$ constants is the crucial value defining the final velocity field. A ratio equal to one allows the same amount of change in horizontal and vertical direction. For ratios $\alpha_h/\alpha_v$ smaller than one, horizontal adjustments are favoured whereas ratios bigger than one mainly allow changes in the vertical. This behaviour allows to connect the $\alpha$ constants to atmospheric stratification. For stable conditions the wind is primarily adjusted horizontally corresponding to a ratio $\alpha_h/\alpha_v > 1$. Unstable conditions are characterized by prevailing vertical adjustments with $\alpha_h/\alpha_v < 1$. $\alpha_h = \alpha_v$ represents neutral stratification with evenly distributed adjustments [Magnusson, 2005]. Ross and Smith [1988] also included topographic features through the Froude number to compute $\alpha$ since the constants also influence on weather air moves around or above an obstacle.

In Sherman [1978] and Dickerson [1978] the value for the Gaussian precision moduli was linked to the observation errors or deviations $\sigma$ of the observed to the adjusted field with $\alpha = 1/2\ \sigma^{-2}$. Sherman states that the value of $(\alpha_v/\alpha_h)^2 = (\sigma_v/\sigma_h)^2$ should be of the same magnitude as the ratio of vertical and horizontal velocity $(w/u)^2$.

All models used in the studies mentioned above use a vertical coordinate system that is based on the geometric height. Therefore horizontal and vertical velocity as well as their adjustments are of comparable magnitude. This model uses a pressure based vertical coordinate where the vertical velocity is constituted in $\eta s^{-1}$. Hence, the vertical velocity is smaller by a factor of $10^{-4}$ compared the horizontal velocities. As a consequence, the parameter controlling the vertical adjustment ($\alpha_\eta$) has to be about four times bigger in magnitude than the horizontal parameters to reach the same results.

For the real cases three different approaches defining $\alpha_\eta$ are taken in this work. As a first approach $\alpha_\eta$ values were varied from 500 to 40000 to find the value that minimizes the difference between the observed and modelled wind field. Then $\alpha_\eta$ is calculated using the approach of

Sherman [1978]:

$$\alpha_\eta = \alpha_x \frac{\sqrt{\sigma_u^2 + \sigma_v^2}}{\sigma_{\omega^*}} \tag{4.4}$$

with $\sigma_u$, $\sigma_v$ and $\sigma_{\omega^*}$ being the standard deviations of the horizontal and terrain following vertical wind velocities. The horizontal transmission coefficient $\alpha_x = \alpha_y$ can be set to 1 because only the ratio between horizontal and vertical coefficients is of importance. In a third attempt, $\alpha_\eta$ is calculated as a linear function of the mean vertical temperature gradient $\partial\theta/\partial z$ to link it with atmospheric stability.

$$\alpha_\eta = k\overline{\frac{\partial\theta}{\partial z}} + d \tag{4.5}$$

The factors $k$ and $d$ have to be chosen empirically. After some testing they were set to $k = 6 \cdot 10^5$ and $d = 10^4$. To compute the vertical gradient, the difference of potential temperature of the fifth ($\approx 150\,\mathrm{m}$) and second level ($\approx 8\,\mathrm{m}$) is divided by the total height difference between both levels. Information about potential temperature is taken from the WRF input data.

The results of the different approaches are compared and discussed for four different case studies in chapter 7.

# Chapter 5

# Idealized Simulation

To validate the behaviour of the mass consistent model, an idealized simulation of a flow over an artificial hill similar to Magnusson [2005] was made. Based on this test setup the resulting wind fields were examined before applying the model to real data.

## 5.1 Model Setup

The model topography has the shape of a Gaussian hill and is given by

$$h_g(i,j) = h_{max} \exp\left(-s\left((i-X_c)^2 + (j-Y_c)^2\right)\right) \tag{5.1}$$

where $h_g$ is the height of the terrain, $h_{max}$ the maximum height of the hill and $s$ the steepness parameter. The variables $i$ and $j$ denote the location of the grid point within the domain and $(X_c, Y_c)$ the central point of the hill. The shape of the hill is shown in Figure 5.1. For this example the height of the hill is set to 500 m and the steepness parameter is $s = 0.08$. The number of grid points in $x$ and $y$ direction is 30 with a grid spacing of 1 km. In the vertical direction 20 levels have been defined with a variable grid spacing similar to Magnusson [2005]. The level-heights are 0 m, 2 m, 4 m, 10 m, 20 m, 50 m, 100 m, 150 m, 200 m, 300 m and 400 m, above 400 m every 200 m up to 2200 m. Since pressure based coordinates are used for this model, the corresponding pressure $p$ to the level heights $z$ is calculated with the barometric formula for an isothermal atmosphere [Bauer et al., 2001]

$$p(z) = p_s \exp\left(-\frac{z}{H}\right) \tag{5.2}$$

with the surface pressure $p_s = 1000\,\text{hPa}$ and the scale height of the atmosphere $H = 8\,\text{km}$.

The input wind field is defined with wind exclusively from the southern direction, therefore $u = \omega = 0$ and $v = 10\,\text{m}\,\text{s}^{-1}$. Below 50 m a logarithmic wind profile for $v$ is defined with

$$v(z) = v_r \frac{\log(z/z_0)}{\log(z_r/z_0)} \tag{5.3}$$

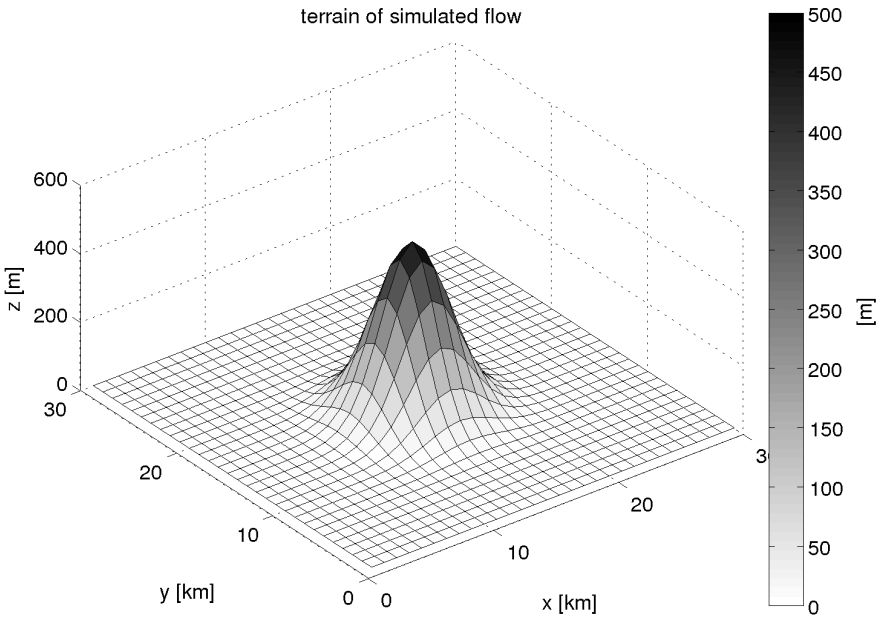


**Figure 5.1:** Gaussian shaped hill for the idealized simulation with a maximum hill size of 500 m.

with a roughness length of $z_0 = 0.01\,\mathrm{m}$, $v_r = 10\,\mathrm{m\,s^{-1}}$ and $z_r = 50\,\mathrm{m}$. At the first level ($z_0 = 0\,\mathrm{m}$) the wind speed is set to zero. The input wind field initially does not "know" the hill. The information about the model terrain is first put in when calculating the terrain following vertical velocity $\omega^*$ with equation (2.48). A vertical cross section of $\omega^*$ through the center of the hill is shown in Figure 5.2 with positive values in front of and negative values behind the hill.

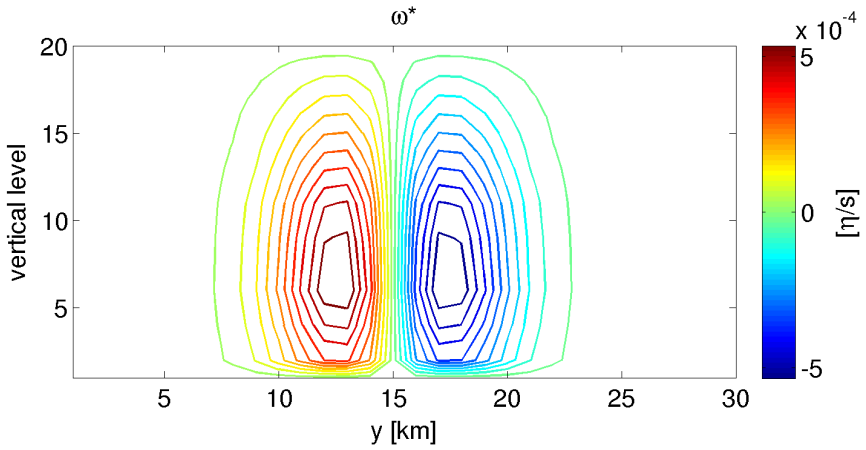


**Figure 5.2:** Vertical cross section of the terrain following vertical velocity $\omega^*$ through the center of the hill calculated from the input wind field.

For the first simulation the $\alpha$-constants were set to $\alpha_x = \alpha_y = 1$ and $\alpha_\eta = 1{\cdot}10^4$. Later three different values for $\alpha_\eta$ are compared.

## 5.2 Results

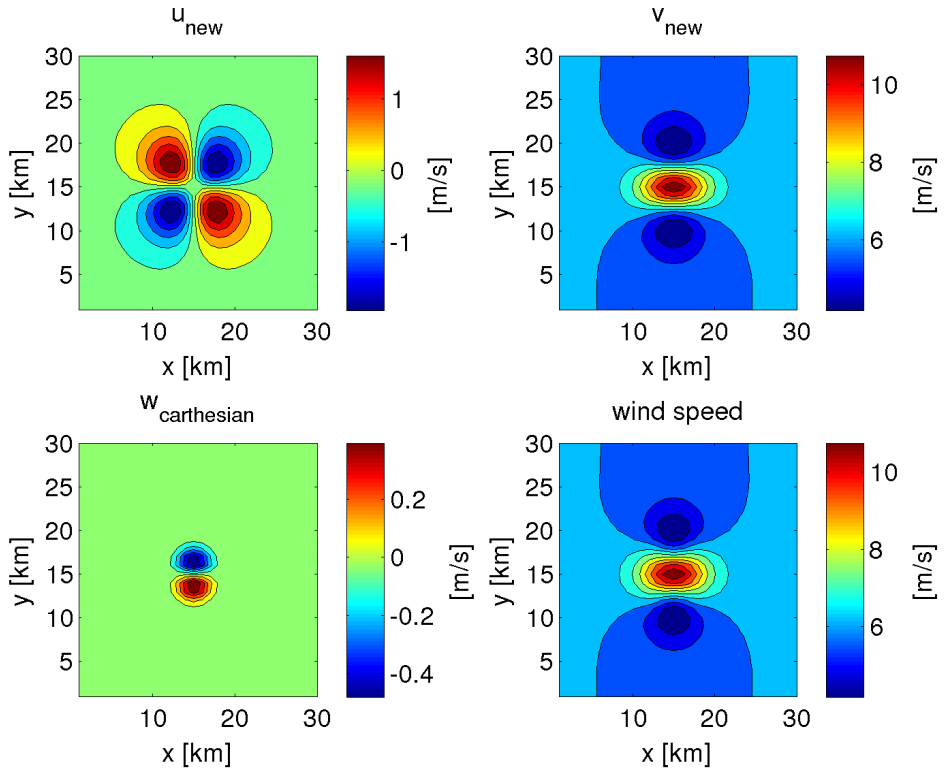


**Figure 5.3:** Adjusted wind components and wind speed at the second vertical $\eta$ level ($\approx 2\,\mathrm{m}$ above ground).

Figure 5.3 shows the resulting horizontal and vertical wind components and the windspeed at approximately 2 m above the ground (second vertical level) after introducing topography as described before and applying the mass consistent model. For the plots the wind speed is calculated as

$$U = \sqrt{u^2 + v^2}. \tag{5.4}$$

with $u$ and $v$ being the wind velocities. To get a more intuitive depiction of the vertical flow component, the terrain following vertical component $\omega^*$ is transformed to cartesian coordinates by first rearranging and applying equation (2.48) and then using the hydrostatic relationship

$$w = -\frac{\omega}{g\rho} \tag{5.5}$$

with $g = 9.81\,\mathrm{m\,s^{-2}}$ and $\rho = 1\,\mathrm{kg\,m^{-1}}$.

The adjustments in the horizontal $u$ component can be seen in the upper left plot. It is easy to see that the flow now goes around the hill. Concerning the vertical velocity component, the lower left plot shows an ascending motion in front of and a descending motion behind the hill. The plots on the right hand side look very similar due to the fact that the $u$ component is much smaller than the $v$ component and the wind speed is calculated according to equation (5.4). In

both plots a deceleration in front of and behind the hill as well as a maximum in the wind speed and $v$ component at the top of the hill can be found.

However, the location of the maximum poses a problem since in reality the maximum in wind speed is located behind the hill. Another error source is the magnitude of the minima which is the same on both sides of the hill for this simulation but can be different in real cases depending on the stratification.

The level of adjustment strongly depends on the choice of the vertical $\alpha$ constant. Figure 5.4b shows streamlines for the same $\alpha_\eta$ value as used in the previous plots. In Figure 5.4a a lower value for $\alpha_\eta$ was chosen which has the effect that the horizontal deflection of the flow is weaker compared with Figure 5.4b. Therefore the vertical adjustment has to be stronger leading to the conclusion that lower values of $\alpha_\eta$ represent unstable stratification whereas higher values reproduce a streaming pattern typical for stable stratification. In Figure 5.4c $\alpha_\eta$ was set to 15000 which results in air rather flowing around than over the artificial hill.

Theoretically, the maximum vertical displacement of an air parcel that approaches an obstacle can be calculated by

$$\delta_{\max} = \frac{u_0}{N} \approx 550\,\mathrm{m} \tag{5.6}$$

with $N$ being the Brunt-Väisälä frequency and $u_0 = 10\,\mathrm{m\,s^{-1}}$ [Markowski and Richardson, 2011]. Air will not be able to flow over a mountain higher than $\delta_{\max}$ because there the stagnation point ($u_0 = 0$) is reached. Hence, for this very stable stratification (isothermal atmosphere) $\alpha_\eta = 15000$ seems to be an appropriate value.

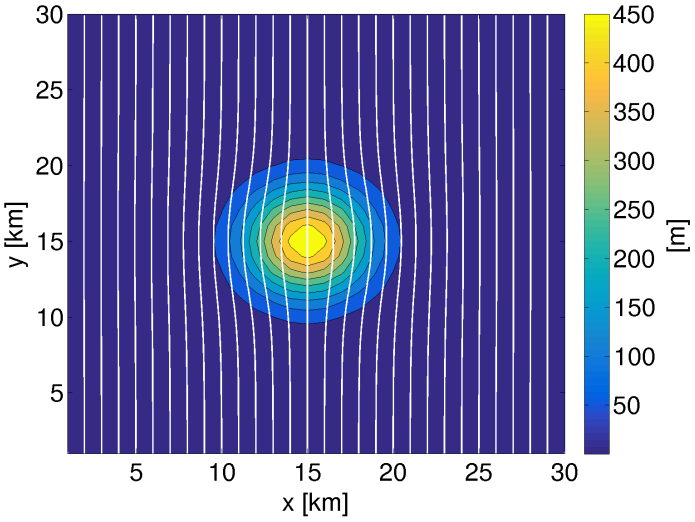


**(a)** $\alpha_\eta = 5000$

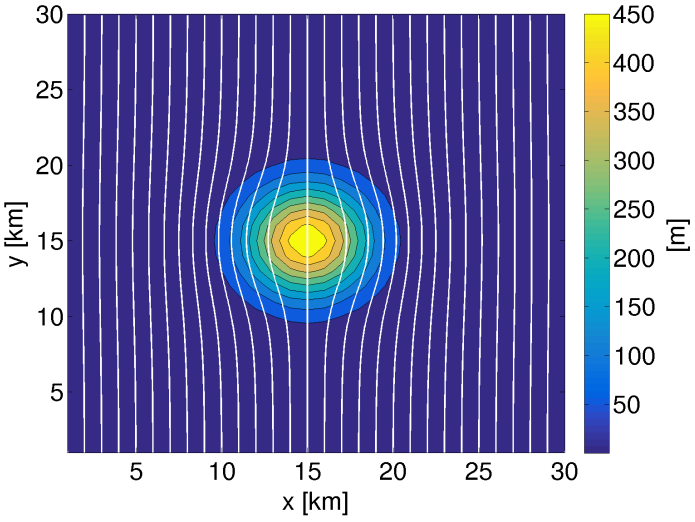


**(b)** $\alpha_\eta = 10000$

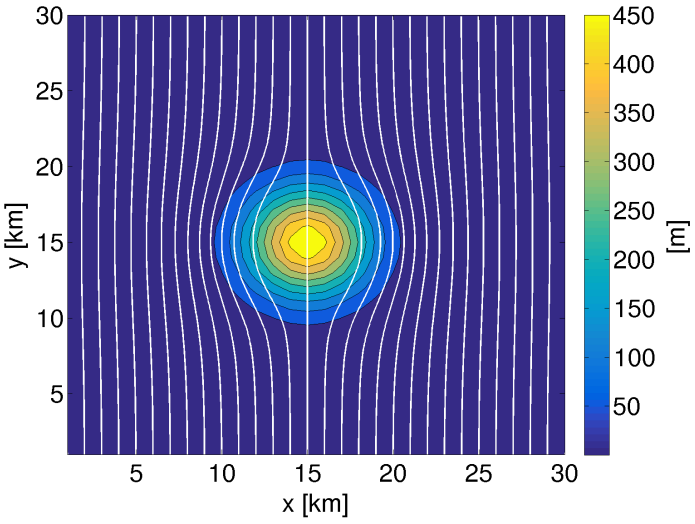


**(c)** $\alpha_\eta = 15000$

**Figure 5.4:** Streamlines of simulated flow for three different values of $\alpha_\eta$ at the second vertical $\eta$ level ($\approx 2\,\mathrm{m}$ above ground).

# Chapter 6

# Real Data and Methods

This chapter describes the data sources used for computing and verifying the mass consistent model. Furthermore the geographical domain used for testing the model as well as the ground based stations within this area are introduced in section 6.2 and 6.3.1. A description of statistical methods, used to compare observed wind data with the interpolated and resulting mass consistent wind fields, is given in section 6.3.2.

## 6.1 The Weather Research & Forecast Model (WRF)

As a first step, prior to running the mass consistent model, input data has to be collected. This data is taken from an operationally used Weather Research and Forecasting (WRF) model with a resolution of 4 km.

The WRF model is a numerical weather prediction and atmospheric simulation system created for both research and operational purposes. It offers a broad spectrum of physics and dynamics options and is therefore applicable for various problems covering all scales from large-eddy to global simulations. Developed by a collaboration between the National Center for Atmospheric Research's (NCAR) Mesoscale and Microscale Meteorology (MMM) Division, the National Oceanic and Atmospheric Administration's (NOAA) National Centers for Environmental Prediction (NCEP) and Earth System Research Laboratory (ESRL), the Department of Defense's Air Force Weather Agency (AFWA) and Naval Research Laboratory (NRL), the Center for Analysis and Prediction of Storms (CAPS) at the University of Oklahoma and the Federal Aviation Administration (FAA), the WRF model is used all over the world in operational services and research with over 6000 registered users [Skamarock et al., 2008].

The WRF Software Framework (WSF) combines the principal components of the WRF system and provides two different dynamic solvers, the Advanced Research WRF (ARW) solver and the NMM (Nonhydrostatic Mesoscale Model) solver. The current ARW Version (Version 3) was first released in April 2008. The equations featured in the ARW solver are fully compressible and non hydrostatic with a hydrostatic option. Amongst some optional variables like turbulent

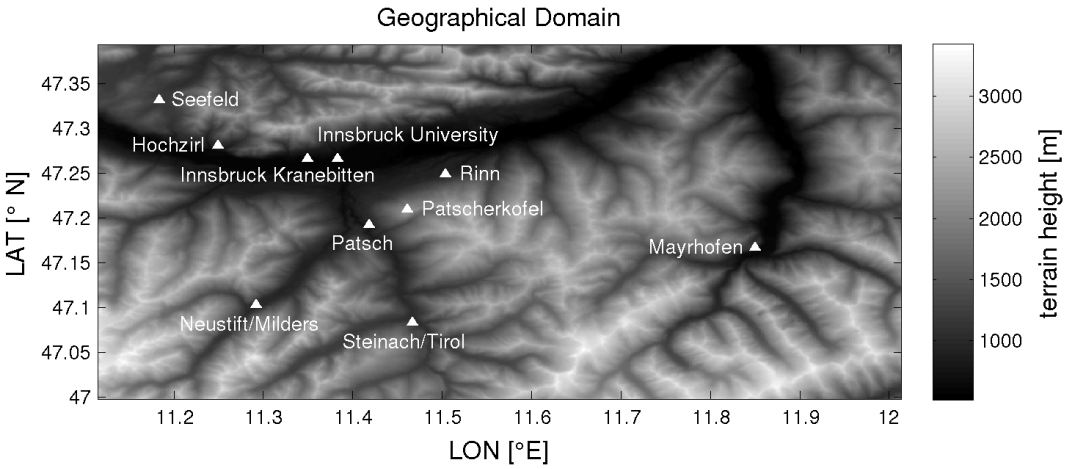


**Figure 6.1:** Map of the domain chosen for testing the mass consistent model including all near ground observation stations used for verification.

kinetic energy or water vapour mixing ratio, prognostic variables include the velocity components $u$, $v$ and $\omega$, perturbation potential temperature, geopotential and surface pressure of dry air. As vertical coordinate a terrain following, dry hydrostatic pressure coordinate is used. For discretization the model uses a second- or third-order Runge-Kutta time integration scheme. Further specifications of the model can be found in Skamarock et al. [2008].

The WRF variables used as input data for the mass consistent model are: latitude, longitude, height of hybrid levels, pressure, temperature, potential temperature, horizontal and vertical velocity components. Additionally, available surface values are used for terrain height, pressure, temperature and potential temperature.

## 6.2 Geographical Domain

The domain chosen for testing the mass consistent model is a region around Innsbruck, the capital city of Tyrol in Austria and lies between latitudes 47° and 47.4°N and longitudes 11° and 12°E. This alpine area is chosen because of its complex topography including deep valleys as well as high mountain ridges. The most prominent valleys within the domain are the west-east oriented Inn valley and the north-south oriented Wipp valley with its junction point around Innsbruck at an elevation of approximately 570 m. The Inn valley is bounded by the Karwendel mountain range to the north with peaks over 2700 m and by the Tuxer and Stubaier Alps with peaks exceeding 3000 m to the south which are separated by the Wipp valley.

An overview over the area including all measuring stations is given in Figure 6.1 and Table 6.1.

## 6.3 Verification

### 6.3.1 Verification Sources

To investigate the quality and accuracy of the mass consistent model the model data is compared to different observation data.

#### Near Ground Observations

The near ground observations are mostly taken from the measuring network maintained by the ZAMG (Zentralanstalt für Meteorologie und Geodynamik). This network contains about 250 semiautomatic weather stations (TAWES) that, besides measuring wind speed and direction, also sample air and soil temperature, dew point temperature, precipitation, pressure and total radiation in 10-minute intervals. Additional measuring stations at Austrian airports are provided by Austro Control (ACG).

The stations that lie within the testing domain (described above) used for verification are listed in Table 6.1.

**Table 6.1:** List of stations within the testing domain used for verification.

| Station Name | Latitude [°E] | Longitude [°N] | Elevation [m] |
|---|---|---|---|
| Innsbruck University | 11.3833 | 47.2667 | 577 |
| Innsbruck Airport | 11.3500 | 47.2667 | 584 |
| Mayrhofen | 11.8500 | 47.1667 | 633 |
| Neustift/Milders | 11.2919 | 47.1028 | 993 |
| Rinn | 11.5039 | 47.2492 | 917 |
| Steinach/Tirol | 11.4667 | 47.0833 | 1025 |
| Patsch | 11.4183 | 47.1928 | 794 |
| Hochzirl | 11.2497 | 47.2809 | 923 |
| Seefeld | 11.1839 | 47.3317 | 1182 |
| Patscherkofel | 11.4617 | 47.2097 | 2247 |

#### Radiosonde Data

For the purpose of verification along the vertical axis, radiosonde data is used. These radio soundings measure temperature, dew point temperature, wind speed and wind direction at specific pressure levels. The only sounding that is available on a regular basis within the domain is the sounding from Innsbruck-Airport (station number 11120) where the radiosonde ascends every day at 3 UTC.

### 6.3.2 Error Measures

Different error measures are used to quantify the performance of the mass consistent model and to compare its result to observational data.

### BIAS

Predictions from numerical weather models can contain systematic errors for various reasons. Among others, systematic errors in wind speed forecasts near the ground can be caused by wrong values for the roughness length or by topographic features not resolved by the model. An error measure for this type of error is the BIAS. For a set of $N$ forecasts, the BIAS is defined as

$$\mathrm{BIAS} = \frac{1}{N}\left[\sum_{i=1}^{N}(\mathrm{H}(F_i) - O_i)\right] \tag{6.1}$$

with $F_i$ being the $i$-th forecast and $O_i$ the corresponding observation. The observation operator H is used in this formula to make different physical quantities comparable - in this work the observation operator is needed to compare observed wind data with gridded wind data by interpolation from the nearest grid point to the location of the measuring station. This provides a measure for the average direction of the deviation from observed values. As a convention, forecast values are subtracted from observed values so that a positive BIAS indicates, on average, a forecast value that exceeds the observations. On the other hand, if the BIAS is negative, the observed value falls below the predicted value on average [Stanski et al., 1989].

Since the BIAS only states the direction but not the magnitude of the error, the BIAS should not be used as a standalone score but be accompanied by other error measures.

### Mean Absolute Error (MAE)

For a series of $N$ forecasts the Mean Absolute Error (MAE) is given by

$$\mathrm{MAE} = \frac{1}{N}\left[\sum_{i=1}^{N}|\mathrm{H}(F_i) - O_i|\right] \tag{6.2}$$

where $F_i$ represents the $i$-th forecast and $O_i$ the corresponding observation [Stanski et al., 1989]. This linear score describes the mean magnitude of the errors but does not give information about the direction of the deviation.

### Root Mean Square Error (RMSE)

The Root Mean Square Error (RMSE) for a series of $N$ forecasts is defined as

$$\mathrm{RMSE} = \left[\frac{1}{N}\sum_{i=1}^{N}(\mathrm{H}(F_i) - O_i)^2\right]^{\frac{1}{2}}. \tag{6.3}$$

$F_i$ and $O_i$ are the $i$-th forecast and observation. Similar to the MAE, the RMSE does not indicate the direction of the deviation since it is always positive. Owing to the square, the RMSE gives more weight to large errors than to small errors. This characteristic leads to a more

appropriate estimation of the error since large errors are particularly unwanted but can also encourage conservative forecasting where forecasts are made near to the climatological mean to avoid large errors.

The RMSE can also be an estimate of the error variance if it is compared to the MAE. A RMSE significantly larger than the MAE indicates a high error variance. If the errors all have the same magnitude, the RMSE has the same value as the MAE. A smaller RMSE can never occur [Stanski et al., 1989].

### Mean Absolute Vector Difference (MAVD)

To compare analyzed and observed wind vectors the mean absolute vector difference is computed [Lotteraner, 2009]:

$$\mathrm{MAVD} = \left[ \frac{1}{N} \sum_{i=1}^{N} (u_o - u_a)^2 + (v_o - v_a)^2 \right]^{\frac{1}{2}} . \tag{6.4}$$

$N$ is the number of stations, $u_o$ and $v_o$ are the components of the observed wind vector and $u_a$ and $v_a$ the components of the analyzed wind vector at the nearest grid point to the observation.

### Spearman Rank Correlation Coefficient

To compare observed and modelled time series of wind speed the Spearman rank correlation coefficient is calculated. It is a technique to evaluate the degree of linear association or correlation of two variables. Since it uses the rank of the data instead of raw data, the influence of outliers on the correlation coefficient is relatively weak. Furthermore this technique is non-parametric so there is no requirement of a specific distribution on the raw data. To compute the rank correlation coefficient each variable is ranked from lowest to highest and the difference between the ranks of each pair of data ($d_i$) is calculated. Then the Spearman rank correlation coefficient ($r_s$) can be calculated by

$$r_s = \frac{1 - 6 \sum_{i=1}^{n} d_i^2}{n^3 - n} \tag{6.5}$$

with $n$ being the number of data pairs [Gautheir, 2001]. The values of $r_s$ can range between 1 (perfect positive correlation) and $-1$ (perfect negative correlation). A correlation coefficient of 0 means that the data is not correlated at all.

### Circular Correlation Coefficient

To get a measure for the correlation of observed and modelled wind direction, a circular correlation coefficient ($\rho$) is used. This coefficient is designed to deal with directional data and can be computed with

$$\rho = \frac{\sum_{i=1}^{n} \sin(\alpha_i - \overline{\alpha}) \sin(\beta_i - \overline{\beta})}{\sqrt{\sum_{i=1}^{n} \sin^2(\alpha_i - \overline{\alpha}) \sin^2(\beta_i - \overline{\beta})}} \tag{6.6}$$

where $\alpha_i$ and $\beta_i$ are two sets of angular data (in polar coordinates) and $\overline{\alpha}$ and $\overline{\beta}$ are the mean values [Berens et al., 2009].

# Chapter 7

# Case Studies

Four different days with different weather conditions (strong gradient, frontal passage, stable and unstable stratification) are chosen to analyze the performance of the mass consistent model within the testing domain (described in section 6.2). As input data simulations from the WRF model with a resolution of 4 km is used. The mass consistent model uses a topography with 500 m resolution.

For every hour of the day the mass consistent wind field is computed. To determine the influence of the $\alpha$ constants on the resulting wind field, several values for $\alpha_\eta$ are used for the simulations. First, different constant values of $\alpha_\eta$, which are chosen empirically, are compared. The chosen values range from 500 to 40000. Another attempt was to couple the value of $\alpha_\eta$ to the standard deviation of the wind components (Eq. 4.4) or the vertical temperature gradient, representing atmospheric stability, (Eq. 4.5). The values of $\alpha_x$ and $\alpha_y$ are set to 1 for all simulations (4.3).

The resulting fields at level 2 of the computational domain, which correspond to a height of approximately 7.65 m above ground, are compared with near ground observations from 10 stations listed in Table 6.1. For this comparison the nearest grid point to the location of the station is used respectively.

For the last case (June, 8th 2015) a WRF simulation with a resolution of 1 km is available. This higher resolved model data is used to compare the performance of diagnostic and prognostic models.

To save some computational time, not all of the 41 vertical levels of the WRF model are used for further computation. Error measures comparing the resulting wind field with observational data are compared for different amounts of vertical levels. For the purpose of retaining high resolution near the ground, the first six vertical levels remain unchanged. Above, only every $\Delta z$-th level is used to calculate the mass consistent wind field. The levels in between are skipped and do not have any influence on the resulting field. Table 7.1 shows the RMSE for wind speed and wind direction and the mean absolute vector difference (MAVD) for different values of $\Delta z$. As an example, these computations are made for March, 31st 2015, 3 UTC. In this case the RMSE and the MAVD show a slight increase when decreasing the number of vertical levels. However,

this behaviour is not found for all dates. When performing the same calculations for 12 UTC, the RMSE of wind direction decreases with lesser vertical levels.

Since different values of $\Delta z$ correspond to changes in higher levels, the 3 UTC sounding of Innsbruck is used to investigate the impact of different amounts of vertical levels. The last column in 7.1 shows the RMSE of wind direction resulting from comparing radiosonde and model data in the vertical column above the nearest grid point to Innsbruck Airport. As expected, this error increases with decreasing vertical resolution. Nevertheless, the general focus is set on lower levels where the errors do not seem to change significantly. Therefore $\Delta z = 5$ has been chosen for all further computations.

| $\Delta z$ | $\mathrm{RMSE_{FF}}$ | $\mathrm{RMSE_{DD}}$ | MAVD | $\mathrm{RMSE_{DD,sounding}}$ |
|---|---|---|---|---|
| 2 | 8.294 | 78.866 | 8.194 | 32.614 |
| 3 | 8.354 | 79.129 | 8.250 | 36.465 |
| 4 | 8.404 | 79.525 | 8.307 | 38.606 |
| 5 | 8.458 | 79.587 | 8.361 | 39.045 |
| 6 | 8.549 | 80.064 | 8.446 | 41.471 |
| 7 | 8.627 | 80.321 | 8.518 | 40.758 |
| 8 | 8.628 | 80.422 | 8.519 | 41.999 |
| 9 | 8.551 | 80.155 | 8.445 | 43.848 |
| 10 | 8.512 | 79.998 | 8.420 | 43.627 |

**Table 7.1:** Root mean square error of wind speed and direction ($\mathrm{RMSE_{FF}}$, $\mathrm{RMSE_{DD}}$) and mean absolute vector difference (MAVD) at the second vertical level and RMSE of wind direction verified with radiosonde data for different numbers of vertical levels used for the computation for March, 31st 2015, 3 UTC with $\alpha_\eta = 10^4$. Every $\Delta z$-th vertical level of the input data is is used for following calculations. The lowest 6 levels are always used.

## 7.1 Case 1 - March, 31st 2015

### Weather Conditions

On this day the weather in Central Europe is characterized by a strong pressure gradient causing strong westerly winds with gusts of over $90\,\mathrm{km\,h^{-1}}$ over parts of Austria, Germany, the Benelux states and the North Sea. A prominent low pressure system, with its core initially located in the north-east of the UK, progresses further west during the day and lies over the Baltic countries 24 hours later. During the day a wave pattern emerges along the Alps with a ridge north west of the Alps and a trough over Italy and south France (see Figure 7.1). This reinforces the pressure difference across the Alps causing higher wind speeds starting around midday. A time series of two stations, Innsbruck Kranebitten and Rinn, is shown in Figure 7.2.

### Results

When looking at the different results for different values of $\alpha_\eta$ one can see the vast impact of the choice of this parameter on the mass consistent wind field. Table 7.2 shows the values of $\alpha_\eta$ that

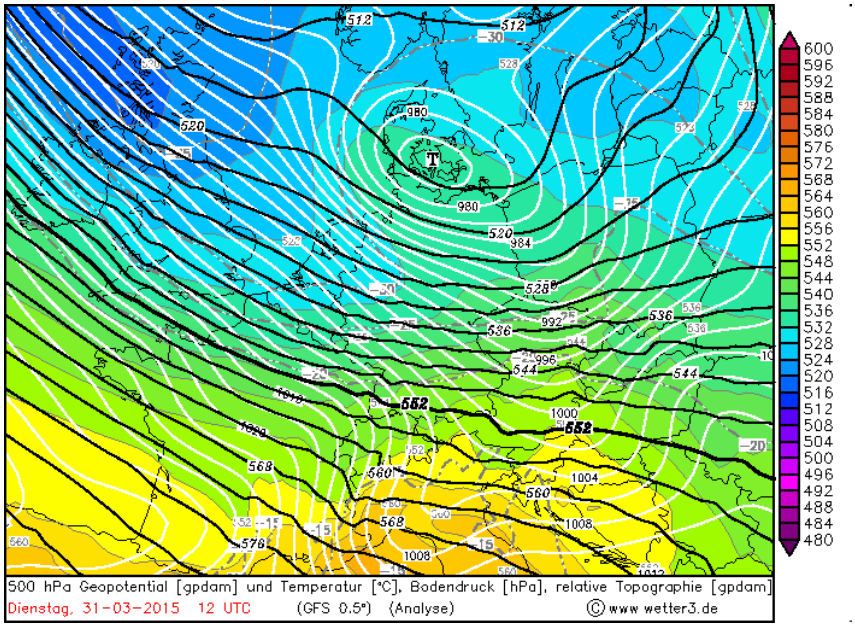


**Figure 7.1:** Synoptic weather conditions for March, 31st 2015, 12 UTC from the GFS analysis with a 0.5° resolution. The black lines indicate the 500 hPa geopotential height in gpdam, white lines the surface pressure in hPa and coloured areas the relative topography (difference of 500 hPa and 1000 hPa (source: `http://www.wetter3.de/Archiv/`).

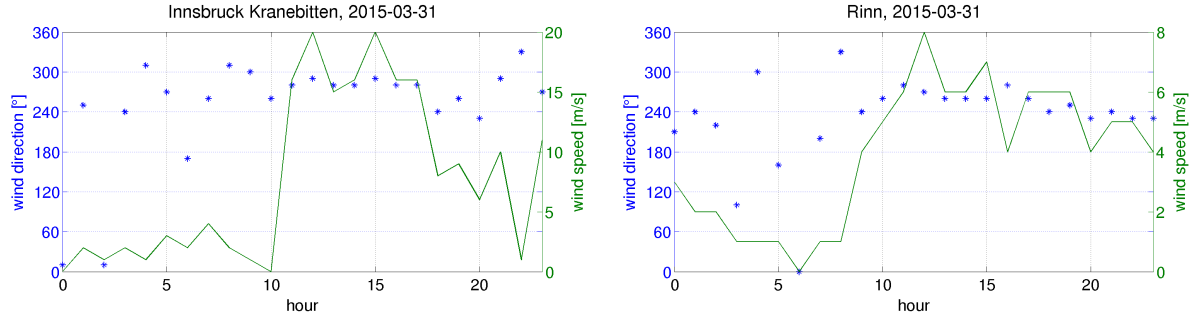


**(a)** Innsbruck Kranebitten (Airport) **(b)** Rinn

**Figure 7.2:** Time series of observed hourly data of wind speed (green) and wind direction (blue) for stations Innsbruck Kranebitten (Airport) and Rinn for March, 31st 2015.

give the lowest error measures compared with observed wind data for several hours of the day. What can be seen at first sight is, that there is no ideal $\alpha_\eta$ that minimizes all errors. There is no hour of the day where the same value of $\alpha_\eta$ minimizes the RMSE for wind speed and direction. Furthermore, the $\alpha$ values computed from the standard deviation of the velocity components or the vertical temperature gradient are often too high. Especially in the night and morning hours, when wind speeds are generally lower and the atmosphere is stably stratified, high values of $\alpha_\eta$ seem to produce winds that are too strong. During daytime, when the atmosphere is well mixed, higher values of $\alpha_\eta$ , corresponding to stronger adjustment of the wind in horizontal direction, are needed to minimize the RMSE of wind speed. When looking at the MAVD, the

best choice for $\alpha_\eta$ is a relatively small value for every hour of the day. These values have the effect of small adjustment in horizontal and stronger changes in the vertical direction.

| | $\alpha_\eta$ for minimal | | | $\alpha_\eta$ computed from | |
|---|---|---|---|---|---|
| hour | $\text{RMSE}_{\text{FF}}$ | $\text{RMSE}_{\text{DD}}$ | MAVD | $\sigma$ (4.4) | $\partial\theta/\partial\eta$ (4.5) |
| 00 | 49113 | 25000 | 49113 | 49113 | 12498 |
| 02 | 500 | 1000 | 500 | 40034 | 17262 |
| 04 | 500 | 35228 | 500 | 35228 | 20464 |
| 06 | 500 | 800 | 500 | 30661 | 19204 |
| 08 | 2000 | 500 | 500 | 30837 | 14258 |
| 10 | 40000 | 9394 | 2000 | 29824 | 9394 |
| 12 | 40000 | 500 | 500 | 30120 | 7891 |
| 14 | 40000 | 500 | 800 | 31515 | 7153 |
| 16 | 30000 | 12000 | 5000 | 31881 | 8478 |
| 18 | 16000 | 30000 | 5000 | 31743 | 10634 |
| 20 | 4000 | 40000 | 2000 | 31665 | 11171 |
| 22 | 3000 | 1000 | 800 | 31819 | 11192 |

**Table 7.2:** $\alpha_\eta$ values resulting in minimal values of RMSE of wind speed ($\text{RMSE}_{\text{FF}}$) and direction ($\text{RMSE}_{\text{DD}}$) and MAVD for every second hour of March, 31st 2015. The two columns on the right show the values of $\alpha_\eta$ computed using the standard deviation of the wind components (eq. 4.4) and the vertical temperature gradient (eq. 4.5).

As an example, we now take a closer look at the wind fields at 10 UTC. According to Table 7.2 the best wind field regarding the minimal value of MAVD is reached for a small value of $\alpha_\eta$ . This means that the flow is adjusted mainly in the vertical. The minimum at $\alpha_\eta = 2000$ can also be seen in Figure 7.3d. For almost the same $\alpha_\eta$ value a minimum is also present in the RMSE of wind speed (Figure 7.3a). But in contrast to the MAVD where the error increases again after the second minimum at $\alpha_\eta = 3\times10^4$ (which is also the $\alpha_\eta$ value computed from (4.4)) the error keeps on decreasing with higher $\alpha_\eta$ leading to an improvement of $\approx 7\%$ compared to the interpolated wind speed. Furthermore, the wind speed shows a positive BIAS which increases strongly at first and then stays more or less constant at a value of approximately $2\,\text{m}\,\text{s}^{-1}$ for $\alpha_\eta > 10^4$ (Figure 7.3c).

Interestingly the BIAS of the mass consistent model is greater than the BIAS of the solely interpolated wind field for all tested values of $\alpha_\eta$. In this case the main advancement is achieved for the wind direction. Compared to the RMSE of the interpolated wind field, the error is reduced by approximately 14° corresponding to an improvement of $\approx 34\%$ for $\alpha_\eta = 10^4$ (Figure 7.3b). The $\alpha_\eta$ value computed from (4.5) is very close to this minimum. However, the best value regarding the wind direction coincides with maximal RMSE for wind speed and MAVD and is therefore overall probably not the best choice.

In Figure 7.4 wind vectors of the interpolated and mass consistent wind field are compared to the observed wind at the available stations for three different values of $\alpha_\eta$. In most of the stations the observed wind speed is generally low. Compared to the observed arrows, the arrows of the interpolated and mass consistent model data are almost always longer. This illustrates the positive BIAS of modelled wind speed mentioned above. Figure 7.4a represents the case

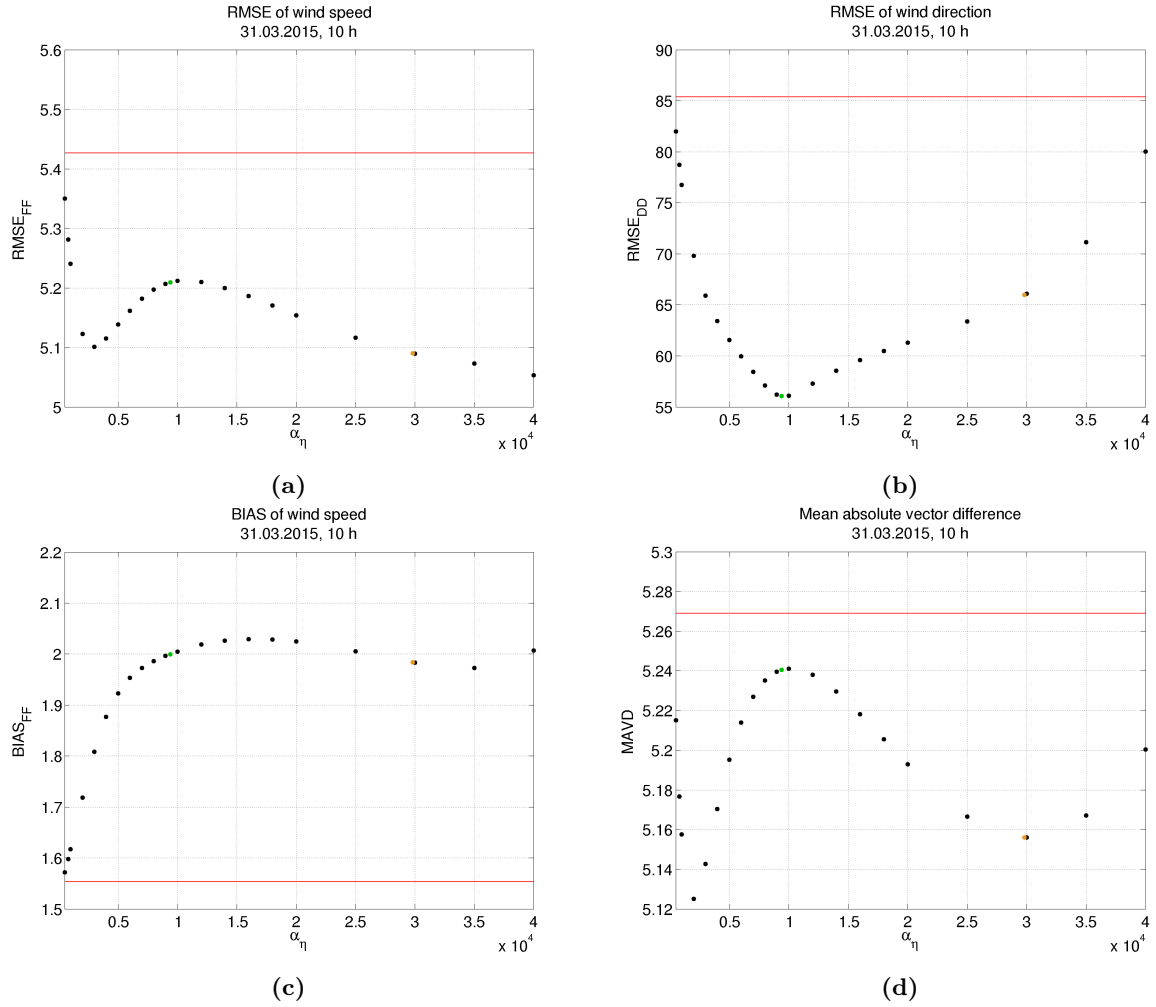


**Figure 7.3:** Different error measures as a function of $\alpha_\eta$ for 10 UTC on March, 31st 2015. The green and blue values mark the $\alpha_\eta$ values computed from (4.5) and (4.4). Red lines represent values for the raw interpolated wind field.

where the MAVD is minimal (cf. Table 7.2). Since this is achieved for a small value of $\alpha_\eta$, the interpolated and mass consistent wind field does not differ much. At some stations the arrows even are congruent. In Figure 7.4b the difference between the modelled wind vectors is already more distinct. The $\alpha_\eta$ value used here is computed from (4.5) and minimizes the RMSE of wind direction. While the improvement for most stations is rather weak, an obvious improvement can be seen at station Patscherkofel. For this station the mass consistent value looks even better in Figure 7.4c where the observed and mass consistent winds almost coincide. There $\alpha_\eta$ was set to $4 \times 10^4$ which is the best value regarding wind speed. Especially station Seefeld shows apparent advance in wind speed (at the cost of almost opposite wind direction).

To further investigate the performance of the model over the whole day time series of wind speed and wind direction at specific stations are shown in Figure 7.5. In addition to this, correlations of observed and modelled time series are computed and shown in Table 7.3 and 7.4. Stations Mayrhofen and Seefeld do not appear in Table 7.4 because the observed wind speed at these stations is below the threshold of $1\,\mathrm{m\,s^{-1}}$, used for computing correlations, for more than half of

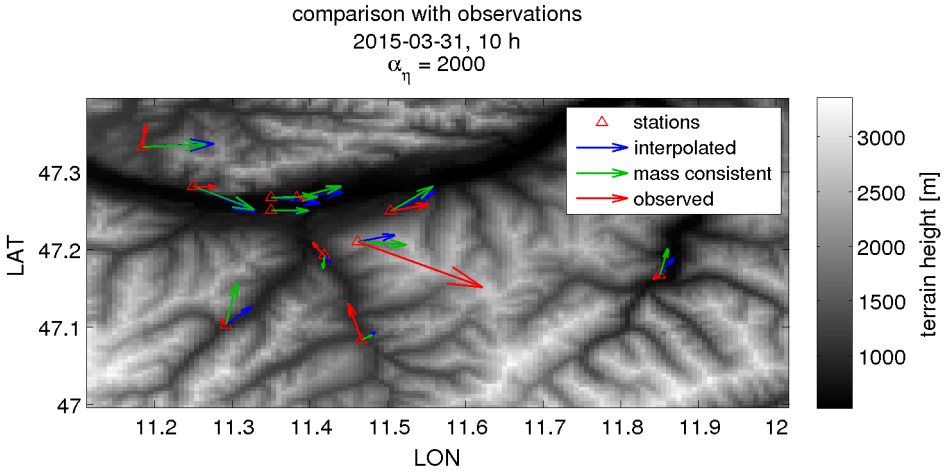


**(a)**

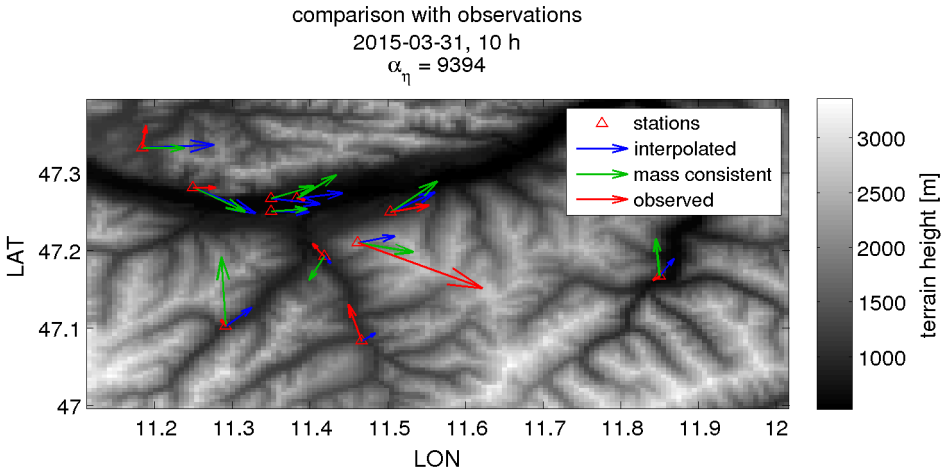


**(b)**

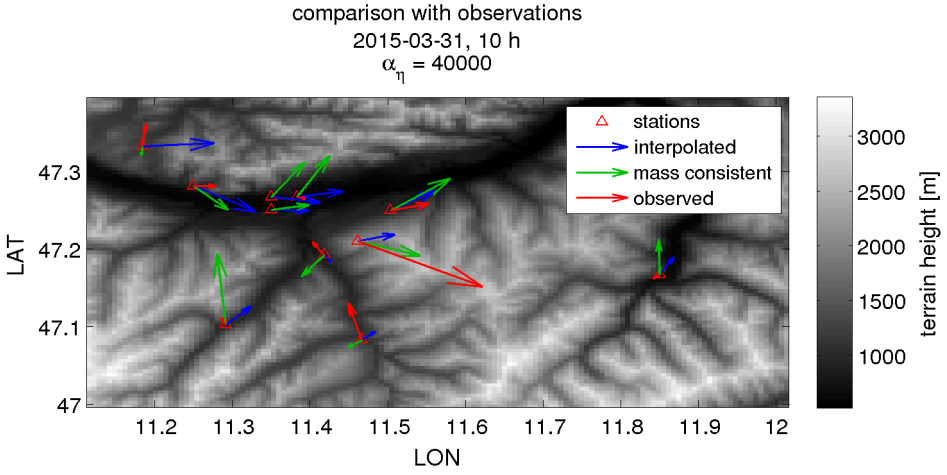


**(c)**

**Figure 7.4:** Comparison of mass consistent (green) and interpolated (blue) with observed wind vectors (red) for different values of $\alpha_\eta$ for March, 31st 2015.

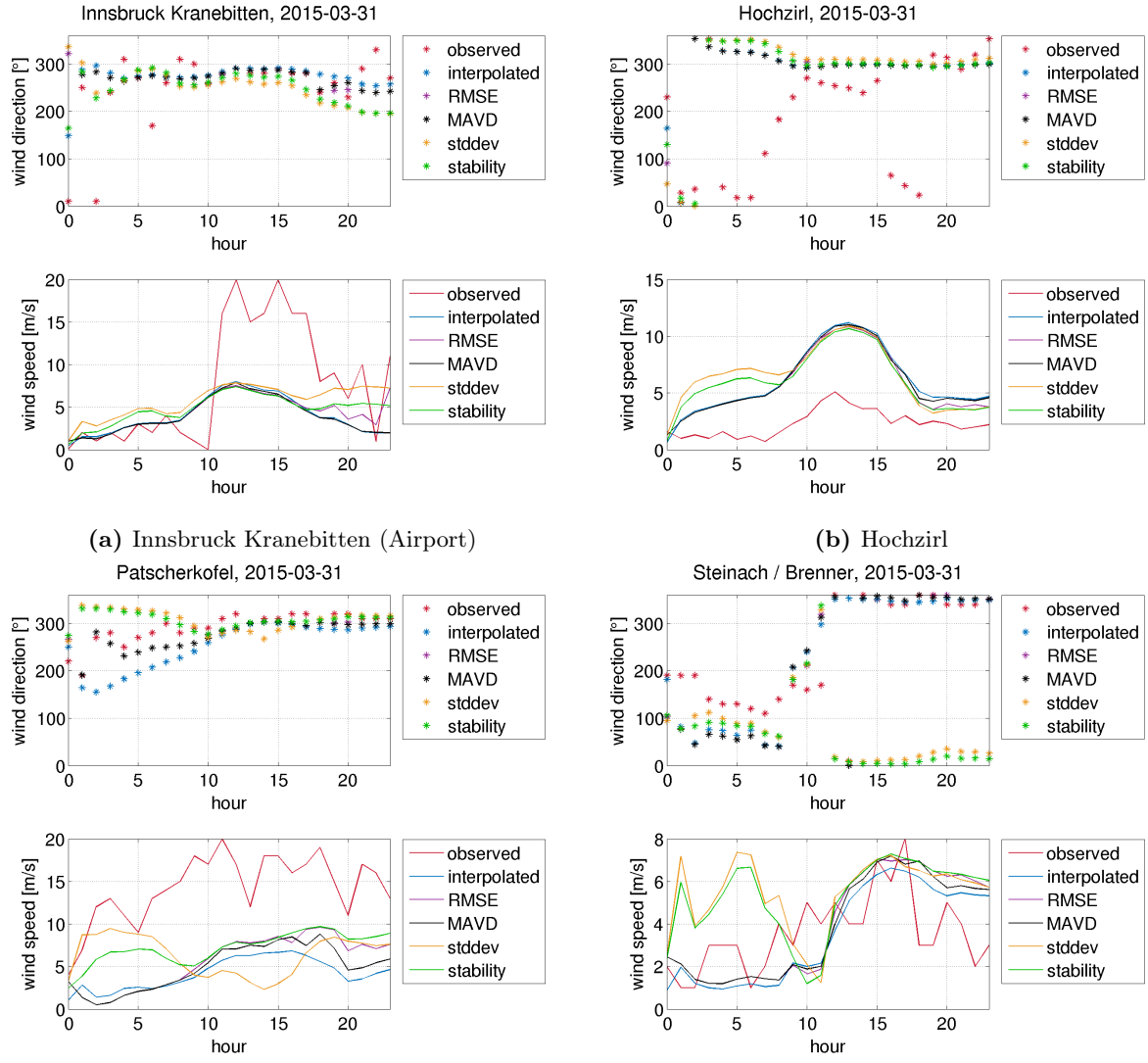


**(a)** Innsbruck Kranebitten (Airport)

**(b)** Hochzirl

**(c)** Patscherkofel

**(d)** Steinach/Brenner

**Figure 7.5:** Comparison of time series for wind direction (top) and speed (bottom) of observed (red), interpolated (blue) and four different mass consistent wind fields (lowest RMSE (purple), lowest MAVD (black), $\alpha_\eta$ from standard deviation (4.4)(yellow) and from stability (4.5)(green)) at four stations for March, 31st 2015.

the day.

For station Innsbruck Kranebitten (Figure 7.5a) highest correlations for wind speed and direction are achieved for the mass consistent model using $\alpha_\eta$ values that minimize the RMSE at every hour. In general the conformity of modelled and observed wind direction gets higher as soon as wind speeds increase (around 10 UTC). Prior to this point observed wind directions show fluctuations that are not captured by the model. Furthermore the model does not reproduce the strong increase in observed wind speed in late morning. Therefore wind speeds are too weak during the second half of the day. Apart from a strong positive BIAS, the shape of the curve of observed wind speed at station Hochzirl (shown in Figure 7.5b) is reproduced well by the model. Therefore also the correlations of wind speed at this station reach high values. This is not the

| | # | interpolated | RMSE | MAVD | stddev | stability |
|---|---|---|---|---|---|---|
| Innsbruck University | 18 | **0.911** | 0.857 | 0.907 | 0.523 | 0.694 |
| Innsbruck Kranebitten | 18 | 0.832 | **0.931** | 0.810 | 0.736 | 0.829 |
| Neustift / Milders | 16 | 0.338 | **0.342** | -0.175 | -0.342 | -0.463 |
| Rinn | 18 | 0.765 | **0.834** | 0.811 | 0.775 | 0.652 |
| Steinach / Brenner | 21 | **0.502** | 0.161 | 0.461 | 0.093 | 0.291 |
| Patsch | 16 | 0.610 | 0.439 | **0.613** | 0.339 | 0.532 |
| Hochzirl | 20 | 0.870 | 0.733 | **0.877** | 0.730 | 0.815 |
| Seefeld | 13 | 0.415 | -0.176 | 0.456 | -0.094 | **0.458** |
| Patscherkofel | 24 | **0.687** | 0.587 | 0.573 | 0.562 | 0.661 |

**Table 7.3:** Spearman correlation coefficients of modelled and observed wind speed for March, 31st 2015. The second column shows the number of data points used for computing the correlations where the observed wind speeds are $> 1\,\mathrm{m\,s^{-1}}$. Bold values mark the highest positive correlations for each station.

case for wind direction where the deviations from the observed values are considerably high. Better concordance in wind direction can be found at stations Patscherkofel (Figure 7.5c) and Steinach/Brenner (Figure 7.5d). In contrast to Hochzirl, modelled wind speed at Patscherkofel (a more elevated station) shows a negative BIAS. Only for the first five hours of the day wind speeds computed with $\alpha_\eta$ values from standard deviation and stability reach roughly similar values. Later the two lines are similar to the interpolated curve. At Steinach/Brenner the same behavior of strong wind speeds during the night and subsequent alignment with the interpolated model can be observed. However, in this case the correlation coefficient of the interpolated model is higher and the mass consistent model can only bring improvement regarding the wind direction.

| | # | interpolated | RMSE | MAVD | stddev | stability |
|---|---|---|---|---|---|---|
| Innsbruck University | 18 | -0.173 | **0.128** | -0.122 | -0.198 | -0.098 |
| Innsbruck Kranebitten | 18 | 0.127 | **0.388** | 0.242 | -0.056 | 0.186 |
| Neustift / Milders | 16 | -0.919 | 0.237 | 0.226 | **0.426** | 0.320 |
| Rinn | 18 | **0.775** | 0.367 | 0.311 | 0.193 | 0.588 |
| Steinach / Brenner | 21 | 0.486 | 0.814 | 0.528 | **0.891** | 0.844 |
| Patsch | 16 | 0.147 | **0.301** | 0.237 | 0.257 | 0.297 |
| Hochzirl | 20 | **0.542** | 0.145 | 0.118 | 0.010 | 0.317 |
| Seefeld | 13 | -0.074 | -0.307 | -0.468 | -0.295 | **0.057** |
| Patscherkofel | 24 | **0.800** | 0.654 | **0.800** | 0.582 | 0.544 |

**Table 7.4:** Circular correlation coefficients of modelled and observed wind direction for March, 31st 2015. The second column shows the number of data points used for computing the correlations where the observed wind speeds are $> 1\,\mathrm{m\,s^{-1}}$. Bold values mark the highest positive correlations for each station.

## 7.2 Case 2 - April, 28th 2015

### Weather Conditions

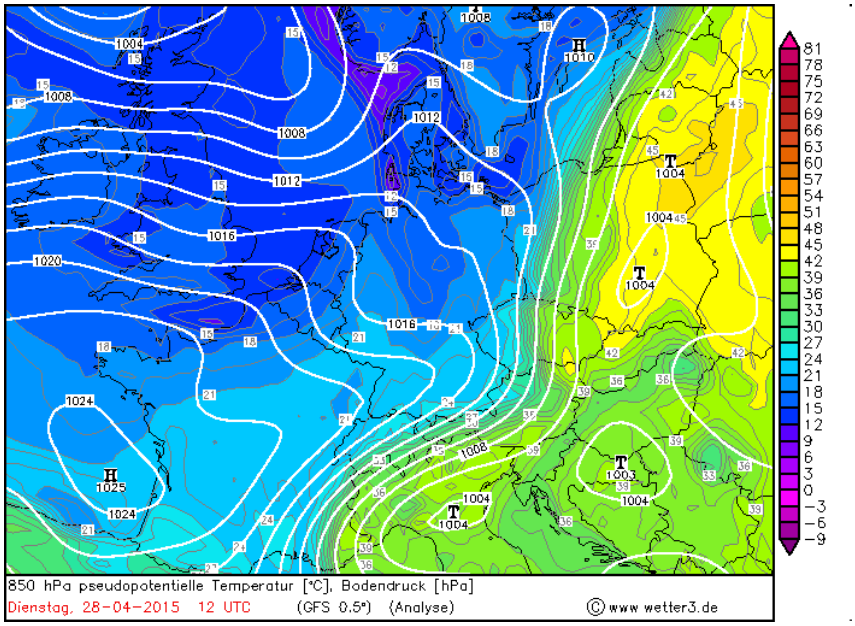


**Figure 7.6:** Synoptic weather conditions in Central Europe for April, 28th 2015, 12 UTC from the GFS analysis with a 0.5° resolution. The coloured areas indicate the pseudopotential temperature in °C, the white lines the surfaces pressure in hPa (source: `http://www.wetter3.de/Archiv/`).

This case is chosen because of the frontal passage happening during the day. The weather situation in Europe is characterized by a complex low pressure system with multiple cores south east of Iceland, in the north of Scandinavia, Austria and in the gulf of Genoa. Originating from a low over Finland a cold front extends over the Baltic countries, through Poland and Germany to the south west of France. During the day, as the front moves further west, it gets blocked by the Alps causing a strong pressure gradient with high pressure north-west and low pressure south-east of the Alps. The transition zone between the air masses at 12 UTC can be seen in Figure 7.6.

### Results

Table 7.5 lists the $\alpha_\eta$ values that result in lowest errors for several hours of the day. Compared to the previous case the optimal $\alpha_\eta$ values for one hour do not differ that much from each other. Apart from the first few hours of the day the variation of $\alpha_\eta$ is relatively small. The generally low values of $\alpha_\eta$ represent more adjustment of the original wind field in the vertical than in the horizontal. When looking at the two right columns of the table one can see that both equations for computing $\alpha_\eta$ from input data lead to values that are too high compared to the ideal values. Nevertheless, using the temperature gradient to calculate $\alpha_\eta$ leads to values that are not too far from ideal during daytime. The dependence of error measures on $\alpha_\eta$ at 12 UTC is investigated in

| | $\alpha_\eta$ for minimal | | | $\alpha_\eta$ computed from | |
|---|---|---|---|---|---|
| hour | $\text{RMSE}_{\text{FF}}$ | $\text{RMSE}_{\text{DD}}$ | MAVD | $\sigma$ (4.4) | $\partial\theta/\partial\eta$(4.5) |
| 01 | 18000 | 500 | 500 | 33862 | 20325 |
| 03 | 25000 | 500 | 500 | 37578 | 17263 |
| 05 | 7000 | 25000 | 8000 | 21368 | 14371 |
| 07 | 3000 | 4000 | 3000 | 17405 | 11667 |
| 09 | 7000 | 3000 | 3000 | 16639 | 10266 |
| 11 | 6000 | 4000 | 5000 | 16326 | 8512 |
| 12 | 7000 | 6000 | 5000 | 16517 | 7909 |
| 13 | 10000 | 3000 | 8000 | 16506 | 7710 |
| 15 | 7000 | 4000 | 5000 | 16574 | 8179 |
| 17 | 6000 | 3000 | 4000 | 17653 | 9408 |
| 19 | 6000 | 16000 | 5000 | 18905 | 10888 |
| 21 | 6000 | 2000 | 5000 | 21023 | 12404 |
| 23 | 1000 | 2000 | 2000 | 24501 | 13543 |

**Table 7.5:** $\alpha_\eta$ values resulting in minimal values of RMSE of wind speed ($\text{RMSE}_{\text{FF}}$) and direction ($\text{RMSE}_{\text{DD}}$) and MAVD for several hours of April, 28th 2015. The two columns on the right show the values of $\alpha_\eta$ computed using the standard deviation of the wind components (eq. 4.4) and the vertical temperature gradient (eq. 4.5).

detail. On the average, the interpolated and the mass consistent model again overestimate wind speed which is reflected in the positive BIAS (Figure 7.7c). However, the BIAS can be reduced for some $\alpha_\eta$ values. In general, in contrast to the previous case (cf. 7.3), all error measures in Figure 7.7 have a distinct minimum that lies below the red line corresponding to the error value of the interpolated wind field. This minimum value almost coincides for all $\alpha_\eta$ values making it possible do determine one ideal $\alpha_\eta$ without making a compromise regarding the resulting wind speed or direction so that an overall improvement can be achieved. Also the value of $\alpha_\eta$ computed from (4.5) is close to the minimum value for all error measures. Similar results are obtained for almost all daytime hours leading to the conclusion that the mass consistent model is able to improve the forecast for this case.

In Figure 7.8 observed winds are compared to interpolated and mass consistent wind vectors. The arrows are shown for $\alpha_\eta = 6 \times 10^3$ leading to a minimal MAVD for 12 UTC (ct. Table 7.5). This value can also be seen as the best overall $\alpha_\eta$ for this hour because it also represents the mean of $\text{RMSE}_{\text{FF}}$ and $\text{RMSE}_{\text{DD}}$. One can see that for most of the stations the wind vector of the mass consistent model is closer to the observed value than the interpolated vector.

Wind vectors of the interpolated and mass consistent model at every fifth grid point are shown in Figure 7.9. Apart from the Inn valley which is resolved by the 4 km grid of the WRF model, the flow of the interpolated wind field is hardly opposed by topography. In contrast, the mass consistent model clearly shows an adaptation to the terrain. Particularly when looking at the smaller valleys like the Wipp or Stubai valley one can see that the wind tends to follow the course of the valleys. This illustrates that the desired feature of the mass consistent model, alignment of the wind field to high resolution topography, is working.

When looking at the time series of some stations within the domain, one can see that the

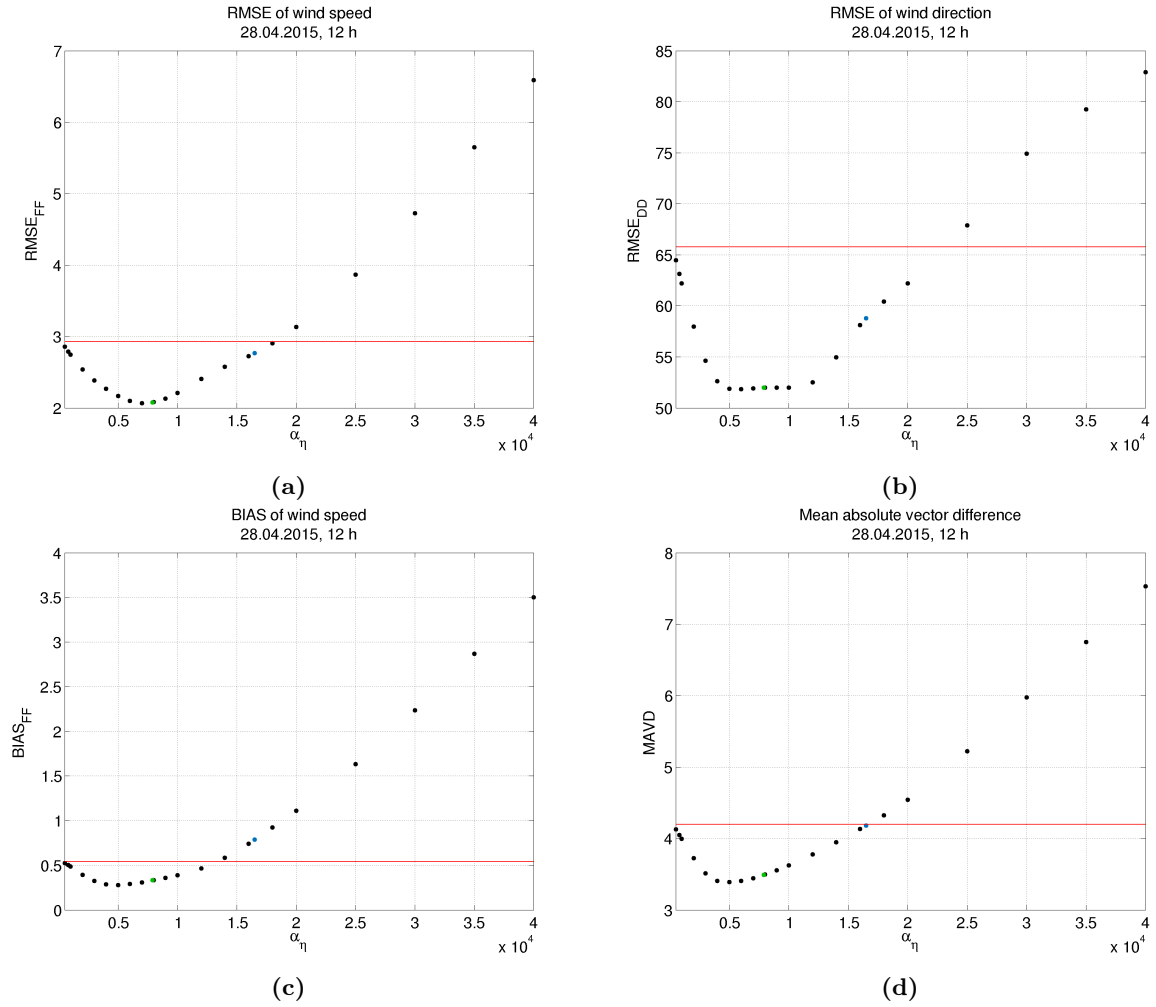


**Figure 7.7:** Different error measures as a function of $\alpha_\eta$ for 12 UTC on April, 28th 2015. The green and blue values mark the $\alpha_\eta$ values computed from (4.5) and (4.4). Red lines represent values for the raw interpolated wind field.

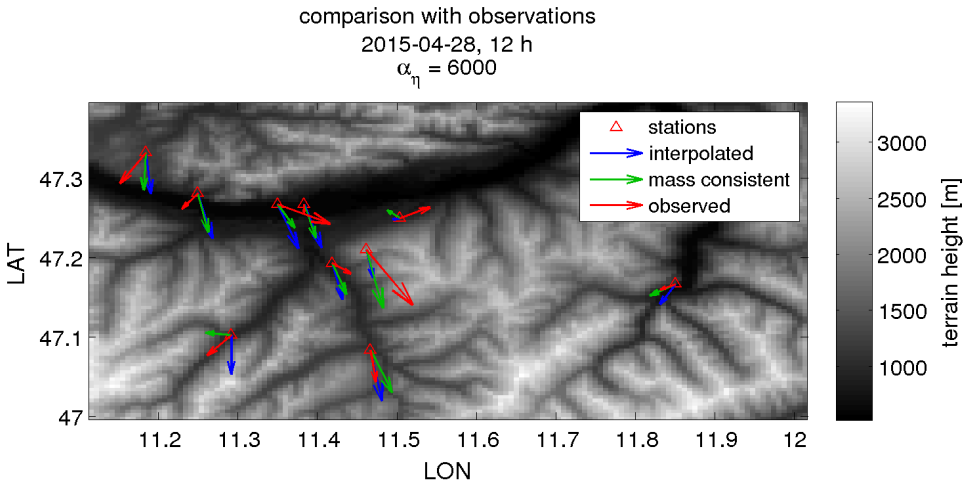


**Figure 7.8:** Comparison of mass consistent (green) and interpolated (blue) with observed wind vectors (red) for $\alpha_\eta = 6 \times 10^3$ for April, 28th 2015 at 12 UTC.

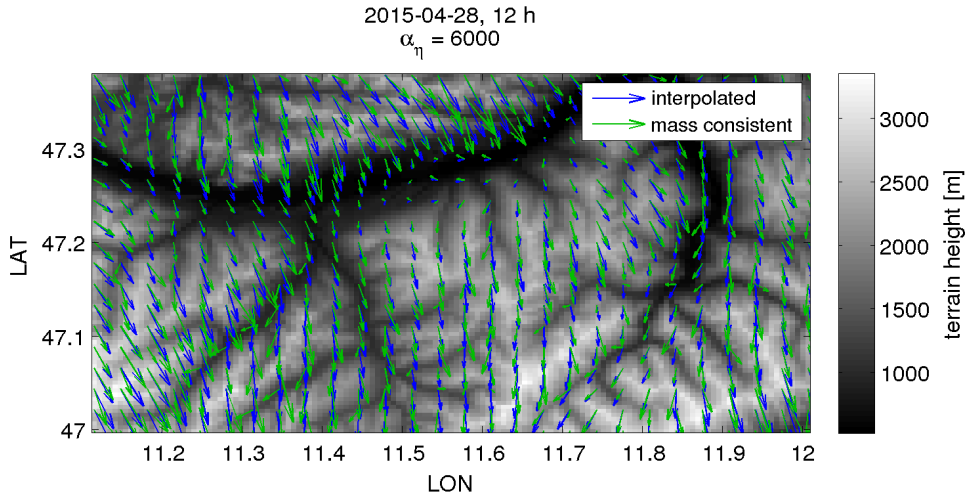


**Figure 7.9:** Comparison of mass consistent (green) and interpolated (blue) wind vectors for $\alpha_\eta = 6 \times 10^3$ for April, 28th 2015 at 12 UTC.

impact and improvement of the mass consistent model differs for every station. None or just very weak improvements can be seen at stations Innsbruck Kranebitten and Rinn whereas for the station Patscherkofel improvements are achieved for both wind speed and direction. The curves representing the mass consistent model show better correlations with the observed values. Especially when looking at the wind speed, the improvement becomes even more distinct. The curve where the $\alpha_\eta$ value is linked to the temperature gradient nearly reproduces the evolution of wind speed over time resulting in a correlation of 0.832 (cf. Table 7.7). The interpolated model underestimates the wind speed at this station for the whole day.

At Neustift/Milders the evolution of wind direction is captured well by the mass consistent model. While the interpolated model shows a clockwise rotation of the wind from West to North in the morning hours, the mass consistent wind follows the observed wind direction. Regarding wind speed, the mass consistent model does not perform that well. The computed $\alpha_\eta$ values are too high and therefore the mass consistent model overestimates wind speed for almost the whole day. Hence, the interpolated model correlates best with the observations.

All correlations of wind speed and wind direction for stations with wind speeds $> 1\,\mathrm{m\,s^{-1}}$ for at least half of the day can be seen in Tables 7.6 and 7.7.

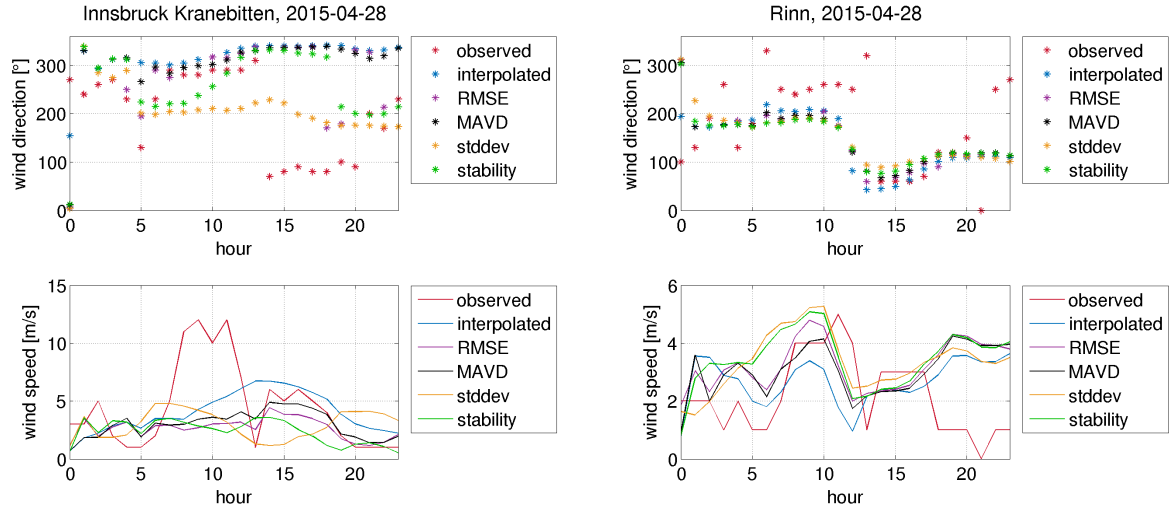


**(a)** Innsbruck Kranebitten (Airport)




**(b)** Rinn

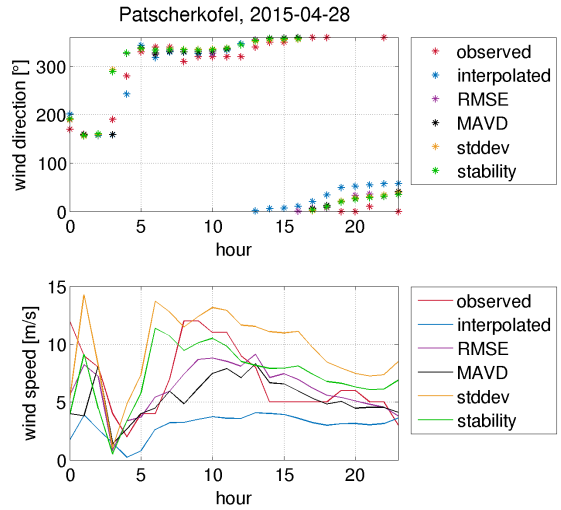


**(c)** Patscherkofel

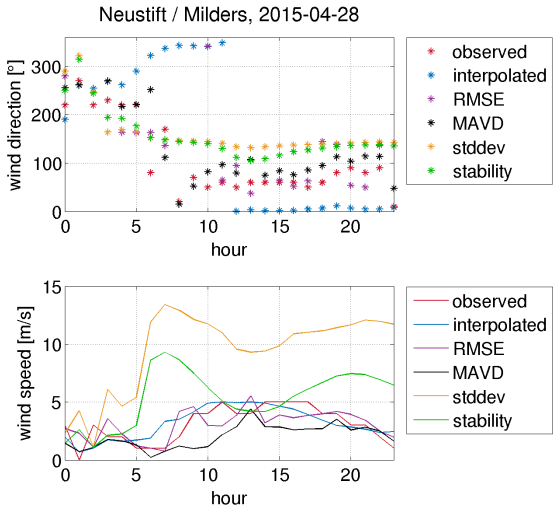


**(d)** Neustift/Milders

**Figure 7.10:** Comparison of time series for wind direction (top) and speed (bottom) of observed (red), interpolated (blue) and four different mass consistent wind fields (lowest RMSE (purple), lowest MAVD (black), $\alpha_\eta$ from standard deviation (4.4)(yellow) and from stability (4.5)(green)) at four stations for April, 28th 2015.

| | # | interpolated | RMSE | MAVD | stddev | stability |
|---|---|---|---|---|---|---|
| Innsbruck University | 16 | 0.744 | 0.718 | **0.759** | 0.363 | 0.629 |
| Innsbruck Kranebitten | 17 | **0.341** | 0.146 | 0.305 | 0.243 | 0.183 |
| Neustift / Milders | 19 | **0.767** | 0.296 | 0.390 | 0.292 | 0.106 |
| Rinn | 14 | -0.115 | 0.446 | 0.324 | **0.543** | 0.376 |
| Steinach / Brenner | 21 | 0.598 | **0.763** | 0.631 | 0.497 | 0.736 |
| Patscherkofel | 24 | 0.336 | **0.692** | 0.459 | 0.428 | 0.397 |

**Table 7.6:** Spearman correlation coefficients of modelled and observed wind speed for April, 28th 2015. The second column shows the number of data points used for computing the correlations where the observed wind speeds are $> 1\,\mathrm{m\,s^{-1}}$. Bold values mark the highest positive correlations for each station.

| | # | interpolated | RMSE | MAVD | stddev | stability |
|---|---|---|---|---|---|---|
| Innsbruck Universtiy | 16 | 0.745 | 0.655 | 0.637 | **0.806** | 0.697 |
| Innsbruck Kranebitten | 17 | **0.624** | 0.162 | 0.345 | -0.480 | 0.227 |
| Neustift / Milders | 19 | -0.506 | 0.321 | **0.808** | 0.649 | 0.680 |
| Rinn | 14 | 0.538 | **0.570** | 0.561 | 0.428 | 0.519 |
| Steinach / Brenner | 21 | -0.464 | -0.219 | -0.359 | **0.099** | 0.040 |
| Patscherkofel | 24 | 0.691 | 0.688 | 0.688 | 0.813 | **0.832** |

**Table 7.7:** Circular correlation coefficients of modelled and observed wind direction for April, 28th 2015. The second column shows the number of data points used for computing the correlations where the observed wind speeds are $> 1\,\mathrm{m\,s^{-1}}$. Bold values mark the highest positive correlations for each station.

## 7.3 Case 3 - May, 11th 2015

### Weather Conditions

A prominent high pressure system lies over central Europe with its core over the Czech Republic and Poland at 6 UTC (see Figure 7.11). Austria is located at the front side of a ridge at 500 hPa leading to stable weather conditions. Due to the weak synoptic forcing wind speeds

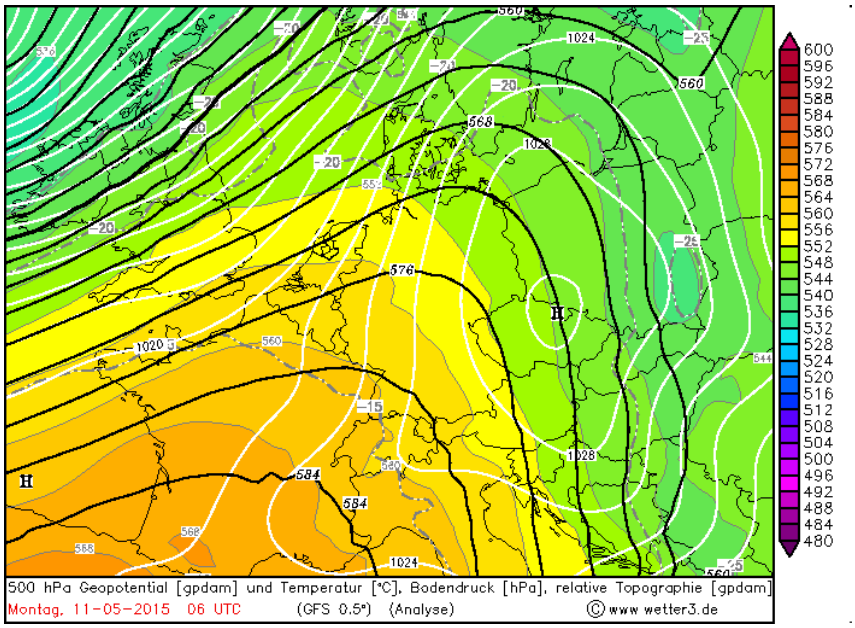


**Figure 7.11:** Synoptic weather conditions in central Europe for May, 11th 2015, 06 UTC from the GFS analysis with a 0.5° resolution. The black lines indicate the 500 hPa geopotential height in gpdam, white lines the surface pressure in hPa and coloured areas the relative topography (difference of 500 hPa and 1000 hPa (source: `http://www.wetter3.de/Archiv/`).

are generally low and the stations within the domain show prevailing thermally driven flows like valley- and slope winds. In Figure 7.13 the time series of wind and wind direction at Steinach is shown where the diurnal cycle of up- and down-valley flow is distinct. During night time and early morning south-easterly winds are observed, corresponding to a down-valley flow of the Wipp valley. During day time the wind direction changes to north west which can be linked to up-valley flow.

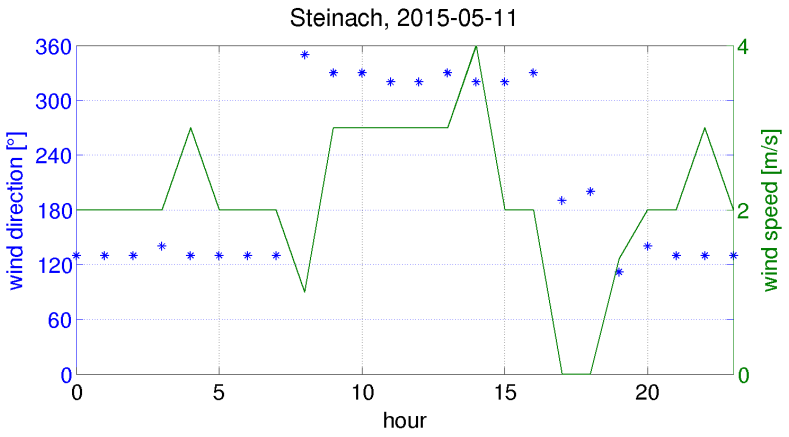


**Figure 7.12:** Steinach/Brenner

**Figure 7.13:** Time series of observed hourly data of wind speed (green) and wind direction (blue) for Steinach/Brenner for May, 11th 2015.

## Results

The $\alpha_\eta$ values listed in Table 7.8 again show a heterogeneous picture. While the $\alpha_\eta$ values that minimize the RMSE of wind speed are high during night and low during day hours, the RMSE of wind direction shows almost an opposite behaviour. The computation of $\alpha_\eta$ from the

| | $\alpha_\eta$ for minimal | | | $\alpha_\eta$ computed from | |
|---|---|---|---|---|---|
| hour | $\text{RMSE}_{\text{FF}}$ | $\text{RMSE}_{\text{DD}}$ | MAVD | $\sigma$ (4.4) | $\partial\theta/\partial\eta$ (4.5) |
| 00 | 9000 | 1000 | 35000 | 58520 | 13394 |
| 02 | 20000 | 8000 | 16000 | 55039 | 24849 |
| 04 | 25000 | 9000 | 5000 | 53762 | 24197 |
| 06 | 500 | 500 | 500 | 56463 | 18194 |
| 08 | 500 | 56956 | 500 | 56956 | 9984 |
| 10 | 500 | 40000 | 12000 | 53012 | 7878 |
| 12 | 500 | 51682 | 8000 | 51682 | 8089 |
| 14 | 500 | 50506 | 500 | 50506 | 9314 |
| 16 | 5000 | 20000 | 500 | 49395 | 10745 |
| 18 | 20000 | 2000 | 3000 | 47911 | 14905 |
| 20 | 25000 | 500 | 4000 | 48786 | 17678 |
| 22 | 25000 | 14000 | 16000 | 48993 | 19001 |

**Table 7.8:** $\alpha_\eta$ values resulting in minimal values of RMSE of wind speed ($\text{RMSE}_{\text{FF}}$) and direction ($\text{RMSE}_{\text{DD}}$) and MAVD for several hours of May, 11th 2015. The two columns on the right show the values of $\alpha_\eta$ computed using the standard deviation of the wind components (eq. 4.4) and the vertical temperature gradient (eq. 4.5).

vertical temperature gradient provides acceptable results during nighttime but during daytime the values are mostly far from ideal. The smallest errors regarding wind directions during the day are achieved with very high $\alpha_\eta$ values (mostly values computed from 4.4). This fits to the

stable weather conditions since high values of $\alpha_\eta$ result in mainly horizontal adjustment of the wind and therefore favour flow around rather than over the mountain.

The evolution of the different error measures with $\alpha_\eta$ is shown in Figure 7.14. Since the behaviour of the errors is broadly similar for all daytime hours, 12 UTC is chosen as an example. As already mentioned above, the errors for wind speed and wind direction have very contrary characteristics. The RMSE (Figure 7.14a) and the BIAS of wind speed (Figure 7.14c) increase whereas the error in wind direction (Figure 7.14b) decreases strongly with greater values of $\alpha_\eta$. If the focus is set on improving wind direction, accepting the positive BIAS of wind speed, the RMSE can be reduced remarkably by more than 35°. If both parameters are of same importance, probably the best compromise is to use the $\alpha_\eta$ value that minimizes the MAVD (Figure 7.14c).

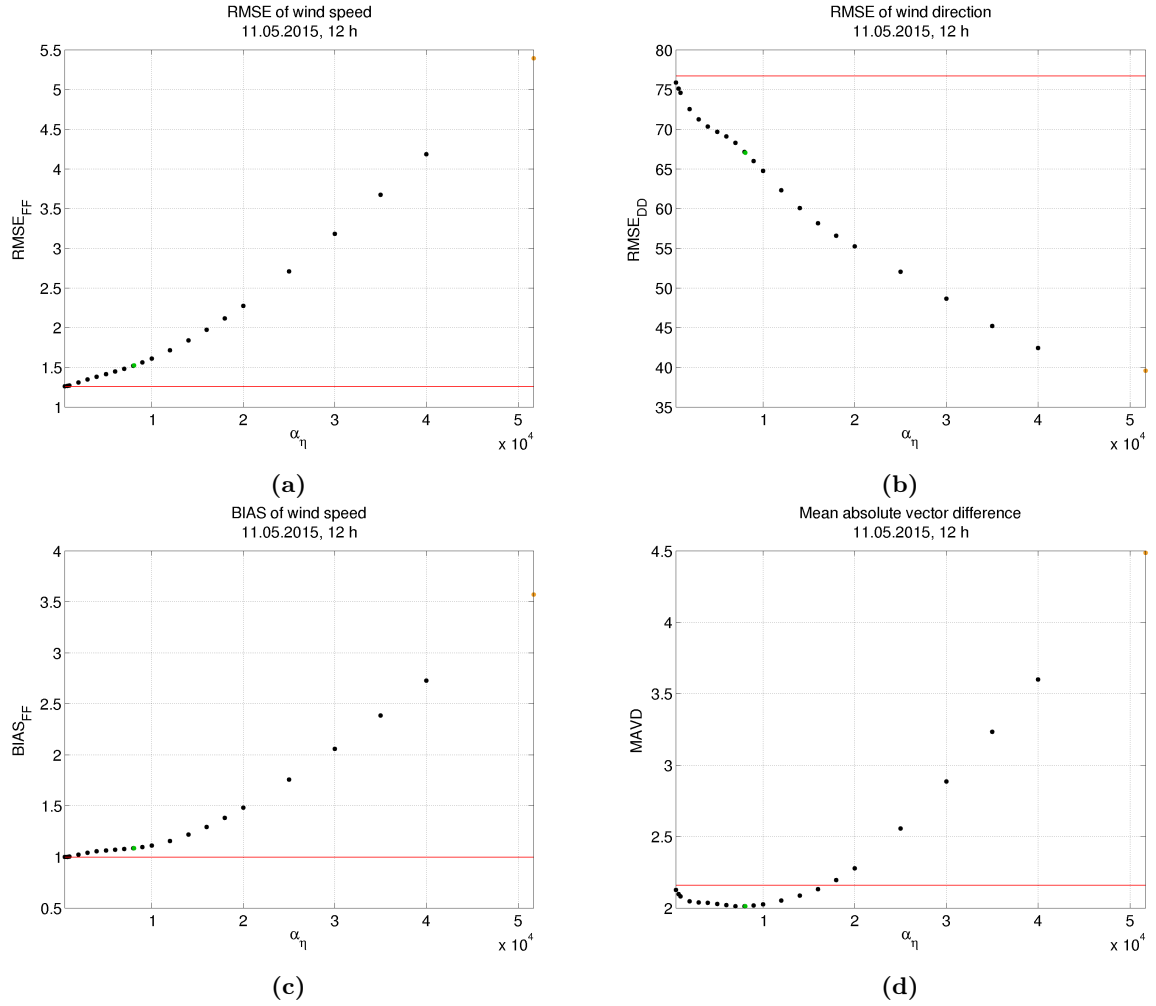


**Figure 7.14:** Different error measures as a function of $\alpha_\eta$ for 12 UTC on May, 11th 2015. The green and orange values mark the $\alpha_\eta$ values computed from (4.5) and (4.4). Red lines represent values for the raw interpolated wind field.

To illustrate the effect of the $\alpha_\eta$ values on the resulting wind field, the wind vectors of the interpolated and mass consistent wind field are compared to the observed wind at the measuring stations. In Figure 7.15a $\alpha_\eta$ was set to 500. According to Table 7.8 this value results in the

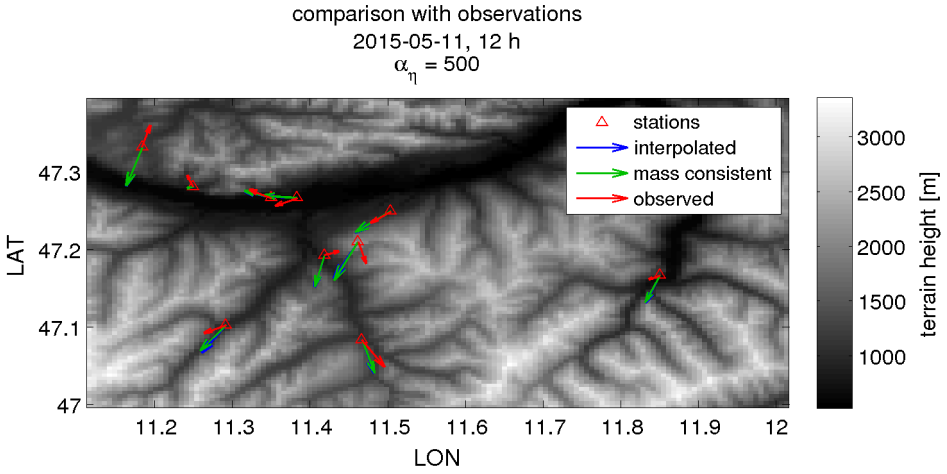


**(a)**

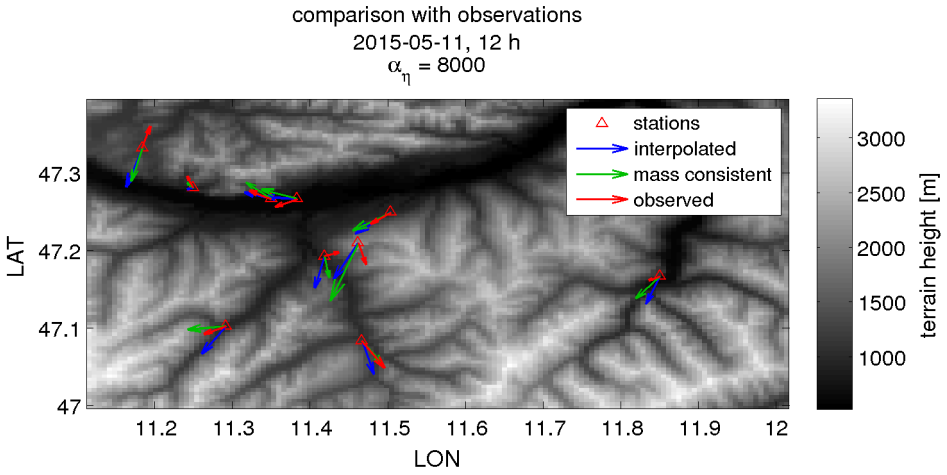


**(b)**

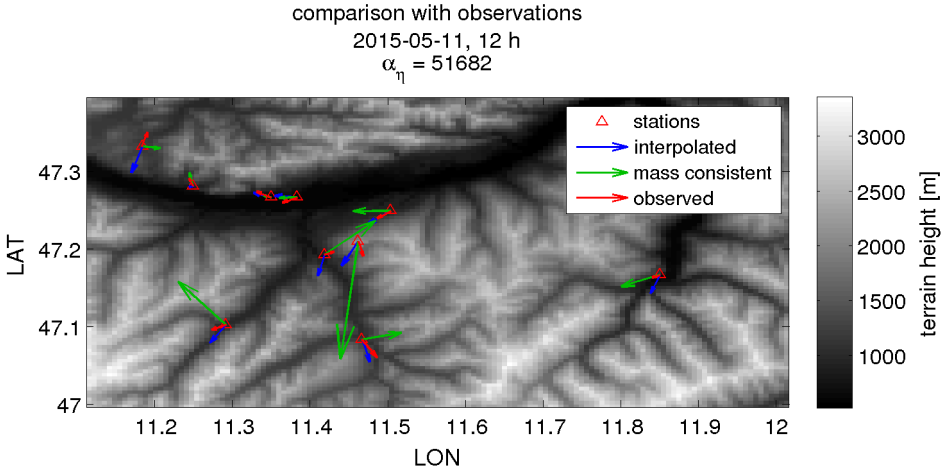


**(c)**

**Figure 7.15:** Comparison of mass consistent (green) and interpolated (blue) with observed wind vectors (red) for different values of $\alpha_\eta$ for 12 UTC on May, 11th 2015.

minimal error for wind speed. The length of the modelled and observed arrows is similar for most of the stations but the mass consistent winds almost show no difference to the interpolated field since the small $\alpha_\eta$ value does hardly allow horizontal adjustment. For $\alpha_\eta = 8 \times 10^3$ (7.15b) the difference of the mass consistent and interpolated model is more distinct.

Even stronger changes of the wind are achieved in Figure 7.15c. The $\alpha_\eta$ value used in this case is computed from 4.4 and leads to the lowest RMSE of wind direction (cf. Table 7.8). A better alignment of the mass consistent with the observed wind vectors is achieved for the majority of the stations. However, this comes at the price of higher errors in wind speed.

The positive effect of the mass consistent model on the wind direction can be seen especially good at station Seefeld (Figure 7.16a). Yet, an appropriate $\alpha_\eta$ value has to be chosen to achieve significant improvements. Here the $\alpha_\eta$ value computed from the standard deviation of the velocity components (eq. 4.4) clearly gives the best result compared to all other time series.

In Figure 7.16b the negative impact of the high $\alpha_\eta$ value can be seen at the time series of wind speed at station Patsch. While the results of the interpolated model as well as the mass consistent model computed with small $\alpha_\eta$ values are close to the observed data, the curve for the model using $\alpha_\eta$ from equation (4.4) shows a strong positive BIAS over the whole day.

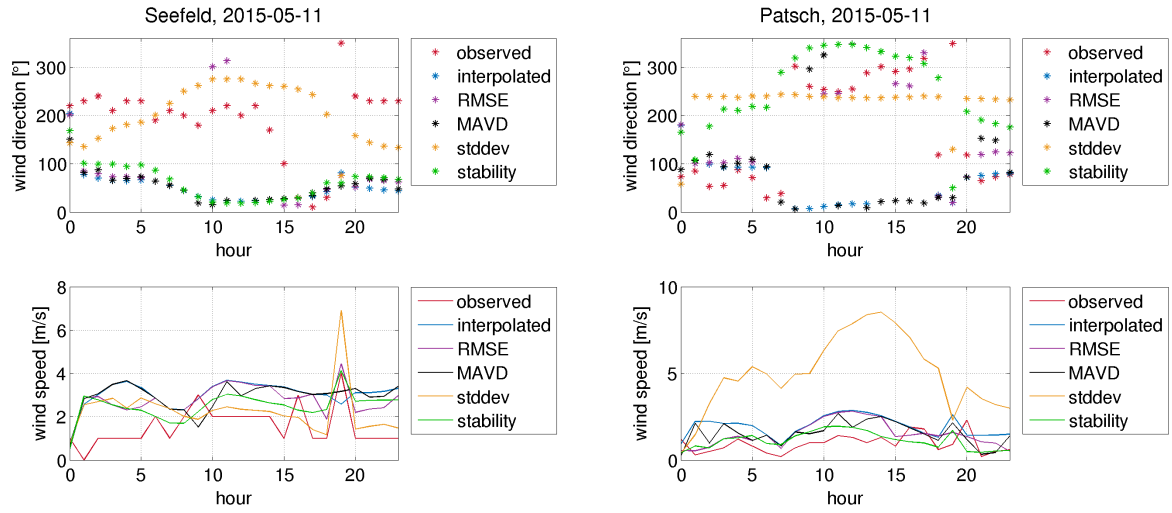


**(a)** Seefeld **(b)** Patsch

**Figure 7.16:** Comparison of time series for wind direction (top) and speed (bottom) of observed (red), interpolated (blue) and four different mass consistent wind fields (lowest RMSE (purple), lowest MAVD (black), $\alpha_\eta$ from standard deviation (4.4)(yellow) and from stability (4.5)(green)) at two stations on May, 11th 2015.

## 7.4 Case 4 - June, 8th 2015

### Weather Conditions

The weather conditions in Central Europe are characterized by a weak pressure gradient. A quasi-stationary cold front, reaching from Russia via Poland and Germany to France, separates cool air masses north of the front from warmer air south of the front. In Austria these warm and high-energy air masses lead to unstable stratification causing thunderstorms to develop during the day. This strong convective activity causes high variability in wind direction and speed. These small scale features of the wind are hard to capture by numerical weather models and almost impossible to resolve by a model using a 4 km grid like the WRF model used as input for the mass consistent model.

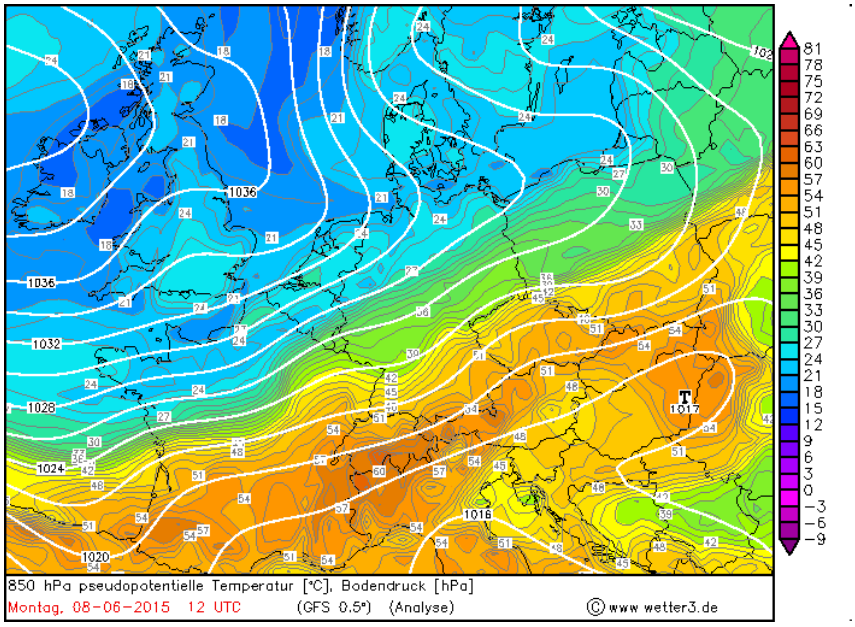


**Figure 7.17:** Synoptic weather conditions in central Europe for June, 8th 2015, 12 UTC from the GFS analysis with a 0.5° resolution. The coloured areas indicate the pseudopotential temperature in °C, the white lines the surface pressure in hPa (source: `http://www.wetter3.de/Archiv/`).

### Results

The $\alpha_\eta$ values minimizing the different error measures show strong variations over the whole day. Only for some hours during the day the optimal $\alpha_\eta$ values for all three error measures coincide with each other or are almost similar. Theoretically one would expect that low values of $\alpha_\eta$ are needed here since they favour stronger adjustments of the flow in the vertical. However, the unstable conditions in the area of interest lead to very variable wind at most of the stations making it hard to determine an ideal $\alpha_\eta$ for this day.

Although the errors in wind speed and wind direction can be minimized for specific values of $\alpha_\eta$,

| | $\alpha_\eta$ for minimal | | | $\alpha_\eta$ computed from | |
|---|---|---|---|---|---|
| hour | $\text{RMSE}_{\text{FF}}$ | $\text{RMSE}_{\text{DD}}$ | MAVD | $\sigma$ (4.4) | $\partial\theta/\partial\eta$ (4.5) |
| 01 | 500 | 40000 | 500 | 26974 | 19128 |
| 03 | 500 | 40000 | 500 | 33910 | 18986 |
| 05 | 18000 | 12000 | 3000 | 33991 | 15005 |
| 07 | 18000 | 40000 | 16000 | 39042 | 9996 |
| 09 | 7000 | 25000 | 20000 | 34357 | 10328 |
| 11 | 18000 | 18000 | 9000 | 23615 | 9951 |
| 13 | 8000 | 40000 | 18000 | 24962 | 10817 |
| 15 | 800 | 12092 | 500 | 22612 | 12092 |
| 17 | 500 | 5000 | 500 | 23701 | 12863 |
| 19 | 30000 | 40000 | 40000 | 26267 | 12895 |
| 21 | 40000 | 20000 | 40000 | 26209 | 13747 |
| 23 | 40000 | 500 | 40000 | 23034 | 12910 |

**Table 7.9:** $\alpha_\eta$ values resulting in minimal values of RMSE of wind speed ($\text{RMSE}_{\text{FF}}$) and direction ($\text{RMSE}_{\text{DD}}$) and MAVD for every second hour of June, 8th 2015. The two columns on the right show the values of $\alpha_\eta$ computed using the standard deviation of the wind components (eq. 4.4) and the vertical temperature gradient (eq. 4.5).

the calculated values in the last two columns of Table 7.9 often are far from ideal. Yet, for some hours an improvement can be achieved. An example is 11 UTC.

With the $\alpha_\eta$ value linked to stability, the mass consistent model can reduce both RMS errors as well as the mean absolute vector difference compared to the interpolated model. Additionally, the BIAS of wind speed can be reduced by both $\alpha_\eta$ values calculated prior to the computations (Figure 7.18c). While the interpolated model has a negative BIAS of $-0.4$, the absolute value of the BIAS can be reduced by the mass consistent model with $\alpha_\eta$ from equations (4.5) and (4.4).

Comparing these results to the errors resulting from the prognostic model with 1 km resolution, one can see that the RMSE of wind direction is significantly lower for the higher resolved WRF model. Furthermore the mean absolute vector difference is slightly smaller. The higher errors in wind speed can be explained by the fact that model data was only available for a height of approximately 30 m and reduced to 10 m using power law

$$v_{10m} = v_r \frac{\log(z/z_0)}{\log(z_r/z_0)} \tag{7.1}$$

where $v_r$ is the wind speed at height $z_r \approx 30\,\text{m}$. The roughness length $z_0$ is set to 2 m.

Taking a look at the time series for different stations within the domain shows that the improvement achieved by the mass consistent model varies from station to station but is generally low.

A constant change of wind direction and speed can be seen at the time series of the station Innsbruck University in Figure 7.19a. The observed wind varies between westerly and easterly directions, corresponding to along-valley wind, that also fluctuates in strength, especially in the afternoon. Since these small scale features can not be resolved by the 4-km-model, also the mass consistent model is not able to reproduce the observed wind. Even for the 1-km-model this

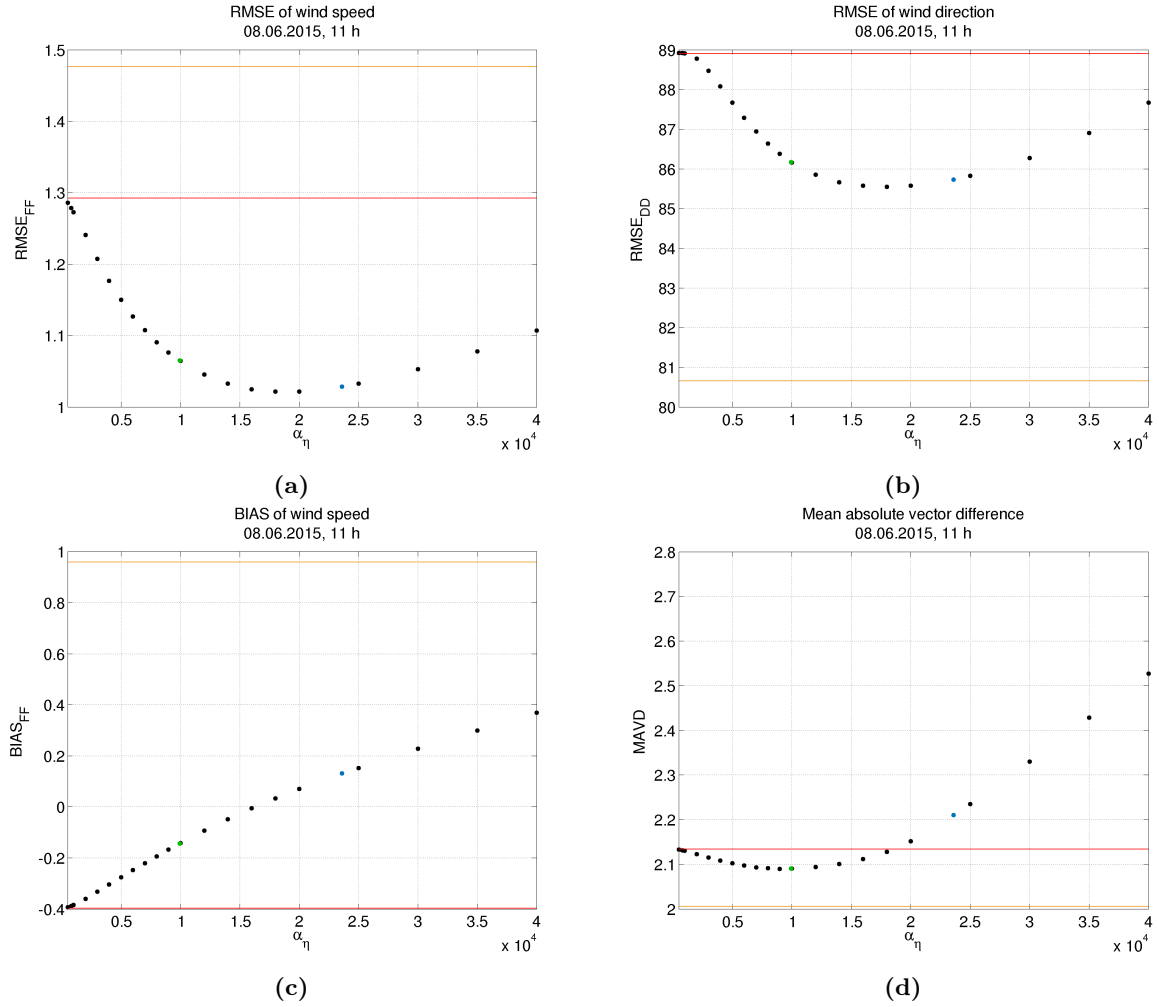


**Figure 7.18:** Different error measures as a function of $\alpha_\eta$ for 11 UTC on June, 8th 2015. The green and blue values mark the $\alpha_\eta$ values computed from (4.5) and (4.4). Red lines represent values for the raw interpolated wind field, orange lines values of the 1 km WRF model.

weather situation is hard to capture and the results can not be improved considerably.
As expected, the correlations of the interpolated as well as the mass consistent winds for this station are not significant with values around 0.1 (cf. Tables 7.10 and 7.11). Correlations with the high resolution prognostic model are even worse for this station.

A slightly better result can be achieved for the station Neustift/Milders located in the Stubaier valley (Figure 7.19b). Here, at least the wind direction shows significant correlation with the observation. However, the mass consistent model does not bring an improvement, the highest correlation is achieved by the interpolated model followed by the 1-km-model. At station Seefeld (Figure 7.19c) the correlation of wind direction is little improved by the mass consistent model. Regarding wind speed as well as both parameters at station Patscherkofel and Innsbruck Kranebitten (Figures 7.19d and 7.19a) the use of the model does hardly bring any benefits.

In general, wind speeds are weak and therefore the threshold for computing correlations, exceeding $1\,\mathrm{m\,s^{-1}}$ at at least 12 hours of the day, is only reached at 5 stations within the domain. The

resulting values are shown in Table 7.10 and 7.11. Interestingly, for this case the 1-km-model does not really improve the forecast.

| | # | interpolated | RMSE | MAVD | stddev | stability | 1-km-model |
|---|---|---|---|---|---|---|---|
| Innsbruck University | 13 | 0.013 | **0.108** | 0.096 | 0.074 | 0.073 | -0.017 |
| Innsbruck Kranebitten | 14 | -0.348 | -0.336 | -0.353 | -0.584 | -0.508 | **0.026** |
| Neustift / Milders | 17 | -0.043 | **0.072** | -0.111 | -0.252 | -0.252 | -0.190 |
| Seefeld | 12 | -0.158 | -0.171 | -0.194 | -0.137 | -0.218 | **0.186** |
| Patscherkofel | 19 | 0.074 | **0.245** | -0.014 | -0.189 | -0.162 | -0.167 |

**Table 7.10:** Spearman correlation coefficients of modelled and observed wind speed for June, 8th 2015. The second column shows the number of data points used for computing the correlations where the observed wind speeds are $> 1\,\mathrm{m\,s^{-1}}$. Bold values mark the highest positive correlations for each station.

| | # | interpolated | RMSE | MAVD | stddev | stability | 1-km-model |
|---|---|---|---|---|---|---|---|
| Innsbruck University | 13 | 0.132 | **0.165** | 0.099 | 0.082 | 0.074 | -0.007 |
| Innsbruck Kranebitten | 14 | 0.044 | 0.118 | **0.169** | 0.020 | 0.160 | -0.300 |
| Neustift / Milders | 17 | **0.660** | 0.467 | 0.481 | 0.343 | 0.505 | 0.582 |
| Seefeld | 12 | 0.094 | 0.218 | 0.328 | 0.299 | **0.343** | -0.163 |
| Patscherkofel | 19 | -0.207 | -0.097 | -0.151 | -0.394 | -0.382 | -0.215 |

**Table 7.11:** Circular correlation coefficients of modelled and observed wind direction for June, 8th 2015. The second column shows the number of data points used for computing the correlations where the observed wind speeds are $> 1\,\mathrm{m\,s^{-1}}$. Bold values mark the highest positive correlations for each station.

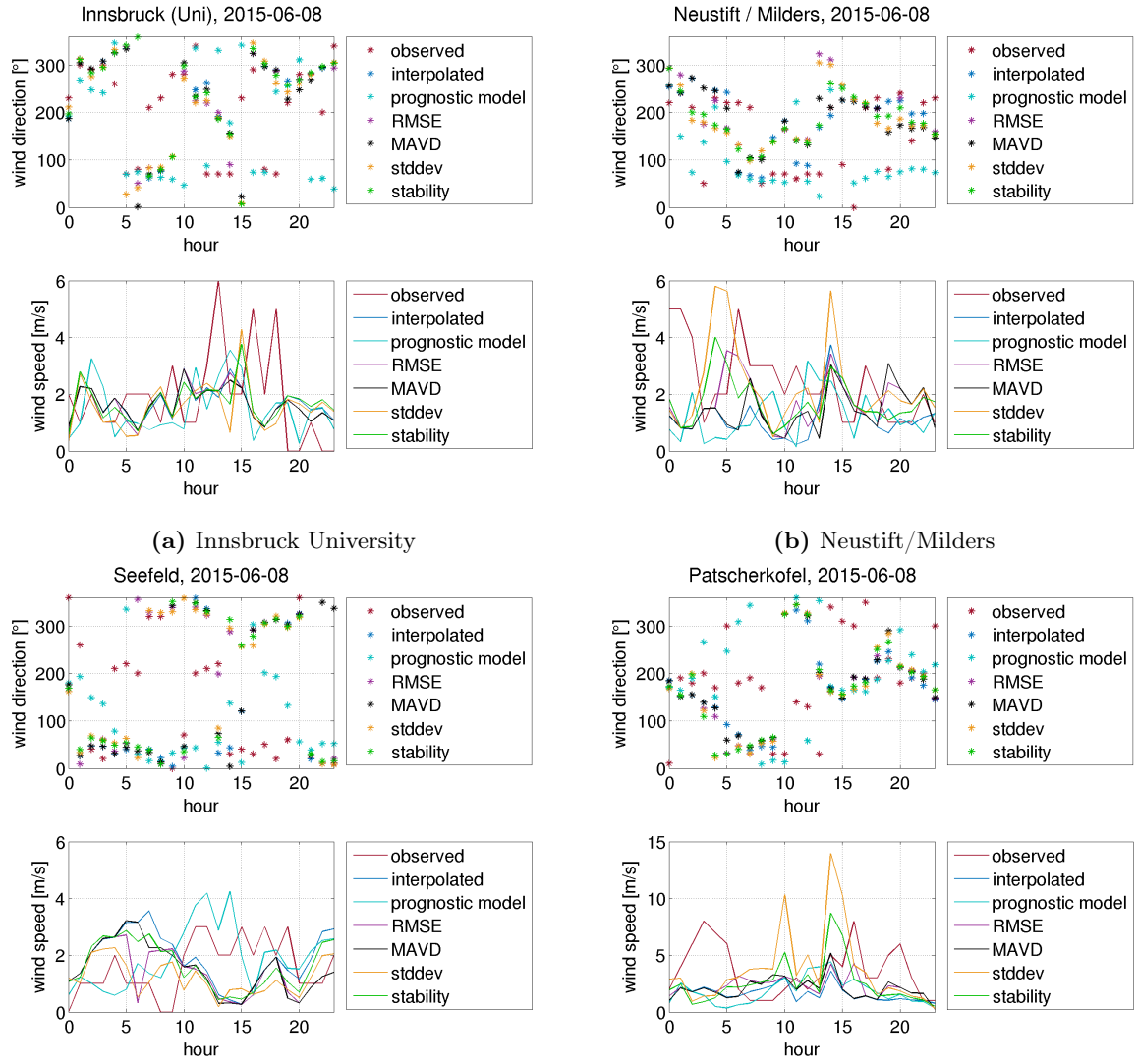


**(a)** Innsbruck University

**(b)** Neustift/Milders

**(c)** Seefeld

**(d)** Patscherkofel

**Figure 7.19:** Comparison of time series for wind direction (top) and speed (bottom) of observed (red), interpolated (blue) and four different mass consistent wind fields (lowest RMSE (purple), lowest MAVD (black), $\alpha_\eta$ from standard deviation (4.4)(yellow) and from stability (4.5)(green)) at four stations on June, 8th 2015.

# Chapter 8

# Conclusion and Future Work

In this work a mass consistent model was developed using $\eta$ coordinates. This brings the advantage of being able to use the output of the operationally used WRF model directly as input data for the mass consistent model. At first, the model was tested in an idealized simulation where it showed reasonable results. Then the model was applied to real data in an area with very complex terrain, a region around Innsbruck, Austria. For that, input data was taken from a 4 km WRF simulation and downscaled to a 500 m grid with more detailed topography. Four case studies representing four different weather conditions were conducted. For all of these cases different values for the vertical transmission coefficient $\alpha_\eta$ were applied and the results compared. Additionally, a prognostic model with a resolution of 1 km was available for comparison for the last case (June, 8th 2015).

## 8.1 Conclusion

This work shows that the mass consistent model can be a useful tool to downscale wind data to a higher resolution topography. Yet, restrictions in the applicability of the model are present and could be shown with the four test cases. Overall, the performance of the model depends on the following factors:

- Resolution and quality of the input data
- Complexity of the underlying terrain
- Prevailing weather conditions
- Choice of the transmission coefficient $\alpha_\eta$ .

For this work the coarse resolution of the input data in combination with the very complex terrain in the tested domain is the main reason for the intermingled performance of the mass consistent model. The 4 km model misses too many important small scale features. Hence, if

features like for example the strong increase in wind speed at station Innsbruck Kranebitten (cf. Figure 7.5a) are not already represented in the coarse grid model, the mass consistent model cannot achieve real improvement. On the one hand, the simple physics of the mass consistent model cannot describe the full dynamics of the meso and micro scale since it only takes into account the continuity equation and the high resolution topography. On the other hand, the level of adjustment made by the model is restricted because in the derivation the assumption is made that the solution closest to the input data, that fulfils mass consistency, is also the most reasonable. Thus, if the wind in the input model differs strongly from the real value, the mass consistent model will not be able to give correct results.

Another important possible error source is the choice of the vertical transmission coefficient $\alpha_\eta$ . In the case studies presented in the previous chapter, ideal values of $\alpha_\eta$ that minimize error measures are computed for every hour of the day. Often the $\alpha_\eta$ values are ideal either for a minimal error in wind speed or in wind direction. Thus, a compromise has to be found or the focus has to be set on only one of the parameters. Yet, when using the model for operational forecasts the best $\alpha_\eta$ value cannot be determined prior to the computations. Therefore, two different approaches on finding an appropriate $\alpha_\eta$ are tried.

Linking the transmission coefficient to the standard deviation of the velocity components often results in $\alpha_\eta$ values that are too high. Especially when considering days with low synoptic forcing, this $\alpha_\eta$ value can cause a strong positive BIAS in wind speed. Good results are achieved in the first case study during day time, where a strong pressure gradient is present. Regarding wind direction, best results are achieved for stable stratification during daytime (case 3).

The calculation of $\alpha_\eta$ from the vertical temperature gradient performs best in the second case where, similar to the first case, a stronger synoptic forcing is present. Here the $\alpha_\eta$ value is close to the values that minimize errors in wind speed and direction. This is the only case in which both parameters can be optimized using almost the same transmission coefficient.

The comparison with the higher resolution prognostic model showed that at least for the selected case the higher computational effort does not lead to better results. However, due to the complex weather conditions on June, 8th 2015 the performance of all models used in this work is generally poor.

Overall, the improvement due to the use of the mass consistent model is highest in terms of wind direction where the RMSE can be reduced by 10° to 30°. The MAVD shows an improvement of 1 % to 15 %. However, decreasing the error in wind direction comes at the cost of an increased wind speed BIAS.

## 8.2 Future Work

For further tests, model output of a higher resolution model can be used as input data. With more small scale processes that can be resolved, this should significantly improve the results over

complex terrain. Additionally, the same 4 km input data could be tested on less complex terrain where small scale processes induced by topography are not that prominent.

Another factor that can be improved is the positive BIAS in wind speed. A possible way to address this problem is to include ground friction to reduce the near ground wind speed. Then higher values of $\alpha_\eta$ can be used to optimize wind direction without the disadvantage of increasing errors in wind speed.

Regarding the $\alpha_\eta$ values, improvements can be achieved by letting the coefficient vary over the whole domain. To implement this change, the dependence of $\alpha_\eta$ on space has to be considered in the derivation. In this work, the $\alpha_\eta$ values are assumed to be constant which leads so some simplifications. With variable $\alpha_\eta$ , changes of atmospheric stratification with height (e.g. inversions) can be considered in the mass consistent model.

Overall, there is room for improvements in many aspects. However, keeping in mind the limits and restrictions in the application of the mass consistent model, it can be an useful instrument to resolve flow over or around topography whose scale is too small to be considered in a prognostic model.

# Bibliography

George B Arfken and Hans J Weber. *Mathematical methods for physicists: a comprehensive guide*. Academic press, 2013.

Siegfried J Bauer, Rudolf Gutdeutsch, Michael Hantel, Heinz Reuter, Helmut O Rucker, Gerold Siedler, Tilman Spohn, Reinhold Steinacker, and Walter Zenk. *Lehrbuch der Experimentalphysik, Bd. 7: Erde und Planeten*. de Gruyter, Berlin, 2001.

Philipp Berens et al. Circstat: a matlab toolbox for circular statistics. *Journal of Statistical Software*, 31(10):1–21, 2009.

Chandrakant M Bhumralkar, Robert L Mancuso, Francis L Ludwig, and David S Renné. A practical and economic method for estimating wind characteristics at potential wind energy conversion sites. *Solar Energy*, 25(1):55–65, 1980.

Robert M Cox, John Sontowski, Richard N Fry Jr, Catherine M Dougherty, and Thomas J Smith. Wind and diffusion modeling for complex terrain. *Journal of Applied Meteorology*, 37 (10):996–1009, 1998.

CG Davis, SS Bunker, and JP Mutschlecner. Atmospheric transport models for complex terrain. *Journal of climate and applied meteorology*, 23(2):235–238, 1984.

Marvin H Dickerson. Mascon-a mass consistent atmospheric flux model for regions with complex terrain. *Journal of Applied Meteorology*, 17(3):241–253, 1978.

RM Endlich, FL Ludwig, CM Bhumralkar, and MA Estoque. A diagnostic model for estimating winds at potential sites for wind turbines. *Journal of Applied Meteorology*, 21(10):1441–1454, 1982.

Sandro Finardi, Maria Grazia Morselli, Pierre Jeannet, et al. Wind flow models over complex terrain for dispersion calculations. In *Cost Action*, volume 710, pages 12–25, 1997.

Thomas D Gautheir. Detecting trends using spearman's rank correlation coefficient. *Environmental forensics*, 2(4):359–362, 2001.

P Geai. Methode d'interpolation et de reconsitution tridimensionelle d'un champ de vent: Le code d'analyse objective minerve. edf, chatou, france. *Report DER/HE/34–87. 03*, 1987.

X Guo and JP Palutikof. A study of two mass-consistent models: problems and possible solutions. *Boundary-Layer Meteorology*, 53(4):303–332, 1990.

Michael Hantel. *Einführung Theoretische Meteorologie*. Springer-Verlag, 2013.

PS Jackson and JCR Hunt. Turbulent wind flow over a low hill. *Quarterly Journal of the Royal Meteorological Society*, 101(430):929–955, 1975.

Hartmut Kapitza and Dieter Eppel. A 3-d poisson solver based on conjugate gradients compared to standard iterative methods and its performance on vector computers. *Journal of Computational Physics*, 68(2):474–484, 1987.

Akira Kasahara. Various vertical coordinate systems used for numerical weather prediction. *Monthly Weather Review*, 102(7):509–522, 1974.

René Laprise. The euler equations of motion with hydrostatic pressure as an independent variable. *Monthly weather review*, 120(1):197–207, 1992.

Christoph Johannes Lotteraner. *Synoptisch-klimatologische Auswertung von Windfeldern im Alpenraum*. PhD thesis, University of Vienna, 2009.

FL Ludwig, JM Livingston, and RM Endlich. Use of mass conservation and critical dividing streamline concepts for efficient objective analysis of winds in complex terrain. *Journal of Applied Meteorology*, 30(11):1490–1499, 1991.

Linus Magnusson. Development and validation of a new mass-consistent model using terrain-influenced coordinates. unpublished, 2005.

Paul Markowski and Yvette Richardson. *Mesoscale meteorology in midlatitudes*, volume 2. John Wiley & Sons, 2011.

Dieter Mayer and Maria Wind. Massenkonsistentes Windmodell in $\eta$-Koordinaten, 2015. Personal Communication.

Dieter Mayer, J Reiczigel, and Franz Rubel. A lagrangian particle model to predict the airborne spread of foot-and-mouth disease virus. *Atmospheric Environment*, 42(3):466–479, 2008.

N Gylling Mortensen, DN Heathfield, Lisbeth Myllerup, Lars Landberg, and Ole Rathmann. *Wind atlas analysis and application program: WAsP 8 help facility (online)*. 2005.

N Moussiopoulos, Th Flassak, and G Knittel. A refined diagnostic wind model. *Environmental Software*, 3(2):85–94, 1988.

GT Phillips. Preliminary user's guide for the noabl objective analysis code. special report, 15 june 1977-15 june 1978. Technical report, Science Applications, Inc., La Jolla, CA (USA), 1979.

Norman A Phillips. A coordinate system having some special advantages for numerical forecasting. *Journal of Meteorology*, 14(2):184–185, 1957.

CF Ratto, R Festa, O Nicora, R Mosiello, A Ricci, DP Lalas, and OA Frumento. *Wind field numerical simulations: a new user-friendly code.* Stephens HS and Associates, Bedford, 1990.

DG Ross and Ian Noble Smith. Diagnostic wind field modelling: development and validation. *Journal of Applied Meteorology*, 27:785–796, 1988.

Yoshikazu Sasaki. An objective analysis based on the variational method. *J. Meteor. Soc. Japan*, 36(3):77–88, 1958.

Yoshikazu Sasaki. Some basic formalisms in numerical variational analysis. *Monthly Weather Review*, 98(12):875–883, 1970.

Christine A Sherman. A mass-consistent model for wind fields over complex terrain. *Journal of applied meteorology*, 17(3):312–319, 1978.

William C Skamarock, Joseph B Klemp, Jimy Dudhia, David O Gill, Dale M Barker, Wei Wang, and Jordan G Powers. A description of the advanced research WRF version 2. Technical report, DTIC Document, 2008.

Henry R Stanski, Laurence J Wilson, and William R Burrows. *Survey of common verification methods in meteorology.* World Meteorological Organization Geneva, 1989.

Kevin E Trenberth, Jeffery C Berry, and Lawrence E Buja. *Vertical interpolation and truncation of model-coordinate data.* National Center for Atmospheric Research, Climate and Global Dynamics Division, 1993.

Ib Troen and Anne De Baas. A spectral diagnostic model for wind flow simulation in complex terrain. *EWEC '86. Proceedings. Vol. 1*, 1987.

# List of Figures